THE ASTROPHYSICAL JOURNAL, 420:721–745, 1994 January 10

THE BALMER-DOMINATED NORTHEAST LIMB OF THE CYGNUS LOOP SUPERNOVA REMNANT

J. JEFF HESTER[1,2]
Department of Physics and Astronomy, Arizona State University, Tempe, AZ 85287-1504
JOHN C. RAYMOND[1,2]
Harvard-Smithsonian Center for Astrophysics, 60 Garden Street, Cambridge, MA 02138
AND
WILLIAM P. BLAIR[1,2]
Center for Astrophysical Sciences, Department of Physics and Astronomy, Johns Hopkins University, Charles & 34th Streets, Baltimore, MD 21218
Received 1992 November 25; accepted 1993 July 22

ABSTRACT

We present a comprehensive investigation of the Balmer-dominated northeast limb of the Cygnus Loop supernova remnant. Data presented include Hα, [O III], and X-ray images, UV and visible spectrophotometry, and high-resolution spectroscopy. The two relatively bright Balmer-dominated filaments visible on the POSS prints are seen to be part of a very smooth and regular complex of filaments. These filaments mark the current location of the blast wave and are seen to bound the sharply limb-brightened X-ray emission, including the previously reported X-ray "halo." The [O III]/Hβ ratio throughout the region is ~0.1, except for regions in which the shock is undergoing a transition from nonradiative to incomplete radiative conditions. At these locations [O III] emission from the cooling region is quite strong, while collisionally excited Balmer-line emission can be weak because of photoionization of the preshock medium by UV from the nascent cooling region. As a result [O III]/Hβ > 100 in some locations. The nonradiative/radiative transition is best studied along the length of the northwestern of the two brightest filaments, where the shock velocity and swept-up column go from ~180 km s^{-1} and 10^{17} cm^{-2} at one end to ~140 km s^{-1} and 8×10^{17} cm^{-2} at the other. There are also a number of locations of such incomplete radiative emission where the shock has recently encountered denser regions with characteristic sizes of ~10^{18} cm.

There is a considerable amount of evidence that the shock has decelerated from ~400 km s^{-1} to less than 200 km s^{-1} in the last 1000 yr. We interpret this as the result of the blast wave hitting the wall of a cavity which surrounded the supernova precursor and succeed in matching a wide range of data with a reflected shock model in which the density of the cavity wall is ~1.2 cm^{-3} and the density in the interior of the cavity is about 0.09 cm^{-3}. This analysis supports previous suggestions that the Cygnus Loop was a cavity explosion. We predict that the X-ray shell will continue to brighten for the next 1000 years or so, during which time the shock front will become radiative throughout the northeast region. The similarity of the time scales for postshock cooling, shock deceleration, and the pressure evolution of the region violates assumptions of steady flow, and greatly complicates interpretation of shock spectra in the region. This may be a common and important effect in many supernova remnants.

High-resolution spectroscopy of the Hα line profile shows that the broad component is surprisingly narrow (~130 km s^{-1}). Consistency between this line width and the shock velocity inferred from spectrophotometry requires either rapid postshock equilibration of T_i and T_e, or that the shock front has decelerated from 180 km s^{-1} to 150 km s^{-1} in the last ~200 yr. While we cannot unambiguously distinguish between these models, the required deceleration is consistent with extrapolation of the shock deceleration rate inferred over the last 1000 years. The width of the narrow component of the Hα line profile is ~33 km s^{-1}, which indicates that the preshock medium has been heated to ~25,000 K by a shock precursor. The most promising types of precursor are heating either by fast neutrals which overtake the shock or by cosmic rays. In the latter case the observed properties of the precursor constrain the cosmic-ray diffusion coefficient to be between about 10^{23} cm^2 s^{-1} and 10^{25} cm^2 s^{-1}. The characteristics of the precursor seem to be about right to explain the presence of weak [S II] and [N II] emission previously reported by Fesen & Itoh (1985).

Morphologically peculiar emission located between the Balmer-dominated filaments and the radiative northeast limb consists of radiative shocks which are less well ordered than the Balmer-dominated region. Interpretation of echelle data gives $\rho v_s^2 \approx 4.3 \times 10^{-10}$ dyn, cm^{-2} for this region, intermediate between the current pressure inferred for the Balmer-dominated shocks and the pressure prior to the blast wave/cavity wall encounter. The morphology of the region may be due to dynamical instabilities in the flow around the edges

[1] Visiting Astronomer Kitt Peak National Observatory, National Optical Astronomy Observatories. The National Optical Astronomy Observatories are operated by the Association of Universities for Research in Astronomy, Inc., under cooperative agreement with the National Science Foundation.

[2] Guest Observer with the *International Ultraviolet Explorer* satellite, which is jointly operated by NASA, the Science Research Council of the UK, and the European Space Agency.

of the cloud responsible for the bright radiative northeast limb. Alternatively, it may represent a phase in the transition of the blast wave from nonradiative to fully radiative during which thermal instabilities are important.

Subject headings: ISM: individual (Cygnus Loop) — ISM: kinematics and dynamics — supernova remnants

1. INTRODUCTION

Nonradiative shock waves seen as faint, pure Balmer line filaments demarcate the edges of 10 supernova remnants (SNRs) and the bow shock for the pulsar PSR 1957+20 (Raymond 1991; Kulkarni & Hester 1988; Aldcroft, Romani, & Cordes 1992). The Hα profiles of these filaments provide unique diagnostics of the shock velocity and the degree of electron-ion equilibration in the postshock gas. This comes about because neutral hydrogen atoms passing through the shock front find themselves immersed in hot plasma where they undergo collisional excitation, ionization, and charge transfer. Excitation of atoms which have not undergone charge transfer leads to an Hα component whose width reflects preshock temperature, while excitations after charge transfer produce a broad component with the kinetic temperature of the postshock ions. The broad component width and the intensity ratio of the broad and narrow components depend on the shock velocity and electron and ion temperatures (Chevalier & Raymond 1978; Chevalier, Kirshner, & Raymond 1980; Smith et al. 1991; Smith, Laming, & Raymond 1993a). When ultraviolet emission lines can be detected, they provide another constraint on the electron temperature (Raymond et al. 1983 [hereafter RBFG]; Fesen & Itoh 1985 [hereafter FI]; Long et al. 1992). This paper and another on Balmer line SNRs in the LMC (Smith, Raymond, & Laming 1993b) show that the narrow component is surprisingly broad, and its width strongly constrains the shock precursor required for diffusive acceleration of cosmic rays (Blandford & Eichler 1987).

The Cygnus Loop is an especially advantageous site for the study of nonradiative shocks. Its large size, high surface brightness, and low reddening make it possible to clearly resolve the nonradiative filaments, detect weak forbidden lines in the optical, and study the UV spectrum in detail (Raymond et al. 1980a, b; RBFG; FI; Long et al. 1992). Deep images reveal a spectacular network of Hα filaments encompassing the northern half of the Cygnus Loop (Hester, Raymond, & Danielson 1986; Hanson & Winkler 1992) as well as other regions in the remnant (Fesen, Kwitter, & Downes 1992). Particularly bright filaments on the east and west limbs were the first to show resolvable narrow components (Treffers 1981; RBFG). Extensive observations from radio (Green 1990) and IR (Braun & Strom 1986) to UV (Benvenuti, Dopita, & D'Odorico 1980; Blair et al. 1991a, b) to X-ray wavelengths (Ku et al. 1984) provide a picture of a 20,000 yr old remnant in a diffuse medium, encountering clouds that are 10–100 times denser (Tucker 1971; McKee & Cowie 1975). The Cygnus Loop has served as a primary test for radiative shock wave models (Cox 1972a; Dopita 1977; Raymond 1979; Shull & McKee 1979; Boulares & Cox 1988) and for theories of SNR evolution (e.g., Cox 1972b) and the interaction between a blast wave and a cloud (Hester & Cox 1986; Raymond et al. 1988; Teske & Kirshner 1985; Ballet et al. 1989).

This paper presents deep Hα and [O III] narrow-band images, *Einstein* HRI images, high- and low-resolution optical spectra, and low-resolution *IUE* spectra of the two brightest nonradiative filaments in the northeast Cygnus Loop. One of these was the subject of ultraviolet investigations (RBFG; Long et al. 1992), and the other shows a clear progression from nonradiative to radiative conditions along its length (Hester & Raymond 1988). We also present new model calculations analogous to those of Smith et al. (1993b) for the line profiles and those of Long et al. (1992) for the spectra, and we derive analytic estimates for the evolution of temperature, density, and depth of the X-ray–emitting gas when a blast wave encounters a large jump in density.

Below in § 2 we present our observations. Models of the line emission from nonradiative shocks as a function of swept-up column depth and models of line profiles for collisionally excited Balmer line emission in the postshock flow are presented in § 3.

In § 4 we discuss our results and present a new global model for the evolution of the blast wave/cavity wall encounter in the Cygnus Loop. Our conclusions are summarized in § 5. Given the amount of data and model results presented, § 5 may serve as a good place to start reading the paper.

2. OBSERVATIONS

2.1. *Imaging*

Images of the vicinity of the brightest Balmer-dominated emission in the northeast Cygnus Loop were obtained in 1986 August using a focal reducing camera on the 1.5 m telescope at Palomar Observatory. The focal reducing system uses a 306 mm collimator and a 58 mm camera lens to reimage a 16′ × 16′ field onto a 800 × 800 Texas Instruments CCD at ∼1.″2 pixel^{-1} and a speed of f/1.65. Figure 1*a* and 1*b* (Plates 14 and 15) show the Hα and [O III] λ5007 images, respectively. The Hα image was obtained through a 15 Å (FWHM) filter; the [O III] image through a 32 Å (FWHM) filter. The Hα image is a single 3000 s exposure. The [O III] image is a composite of two exposures, for a total exposure time of 16,000 s.

The images were obtained using narrow-band interference filters placed in the collimated beam. This has two effects on the data. The first is that light reflected from the CCD is recollimated by the camera lens, partially reflected by the filter, and then refocused on the chip at a point which is the reflection through the optical axis of the position of the original image. Thus all of the bright stars have associated ghost images. The fact that these images are not themselves pointlike shows that the collimator was not perfectly focused. The very faint "filaments" in the extreme northeast corner of Figures 1*a* and 1*b* are likewise ghosts of the bright emission in the southwest. Ghosts of stars have been largely removed from the [O III] image during combination of the two slightly offset [O III] exposures.

The second effect of placing interference filters in the collimated beam is that the filter bandpass changes with distance from the center of the field (just as in an imaging Fabry-Perot). This effect is very pronounced in the Hα image, where the filter bandpass shifts completely off the line in the corners of the field. (The emission in the southwest corner of the field is [N II] λ6548 which is coming through the blueshifted response of the tilted Hα filter.) The flatness of both frames, especially the

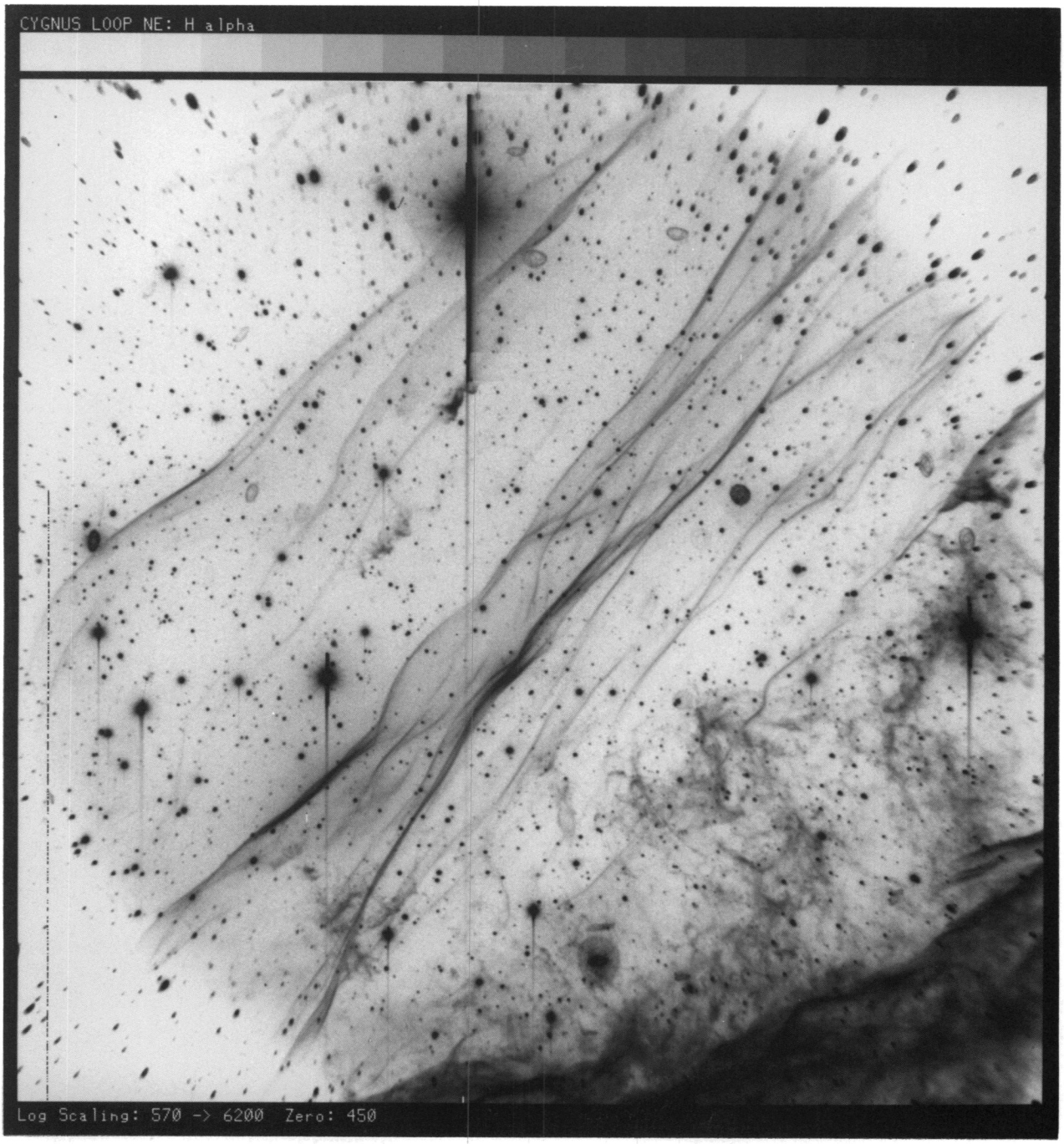

FIG. 1*a*

FIG. 1.—(*a*) An Hα image of a field in the Balmer-dominated northeast limb of the Cygnus Loop supernova remnant. The field shown is 16′ × 16′ and has a sensitivity (3 σ in a 3 × 3 pixel box) of 4.5×10^{-7} ergs cm^{-2} s^{-1} sr^{-1}. The display is logarithmic and goes from below sky to saturation at 2.8×10^{-3} ergs cm^{-2} s^{-1} sr^{-1}. North is at the top of the field and east is to the left. The numerous bubble-like structures are ghosts of star images. The faint "filaments" in the extreme northeast corner of the field are likewise reflections of the bright emission in the southwest. The two brightest filaments, located in the southeast and central portions of the field, are referred to in the text as filaments 1 and 2, respectively. (*b*) An [O III] λ5007 image of the same field as Fig. 1*a*. The sensitivity of the image is 1.7×10^{-7} ergs cm^{-2} s^{-1} sr^{-1}. The display is logarithmic, with saturation at 6×10^{-4} ergs cm^{-2} s^{-1} sr^{-1}.

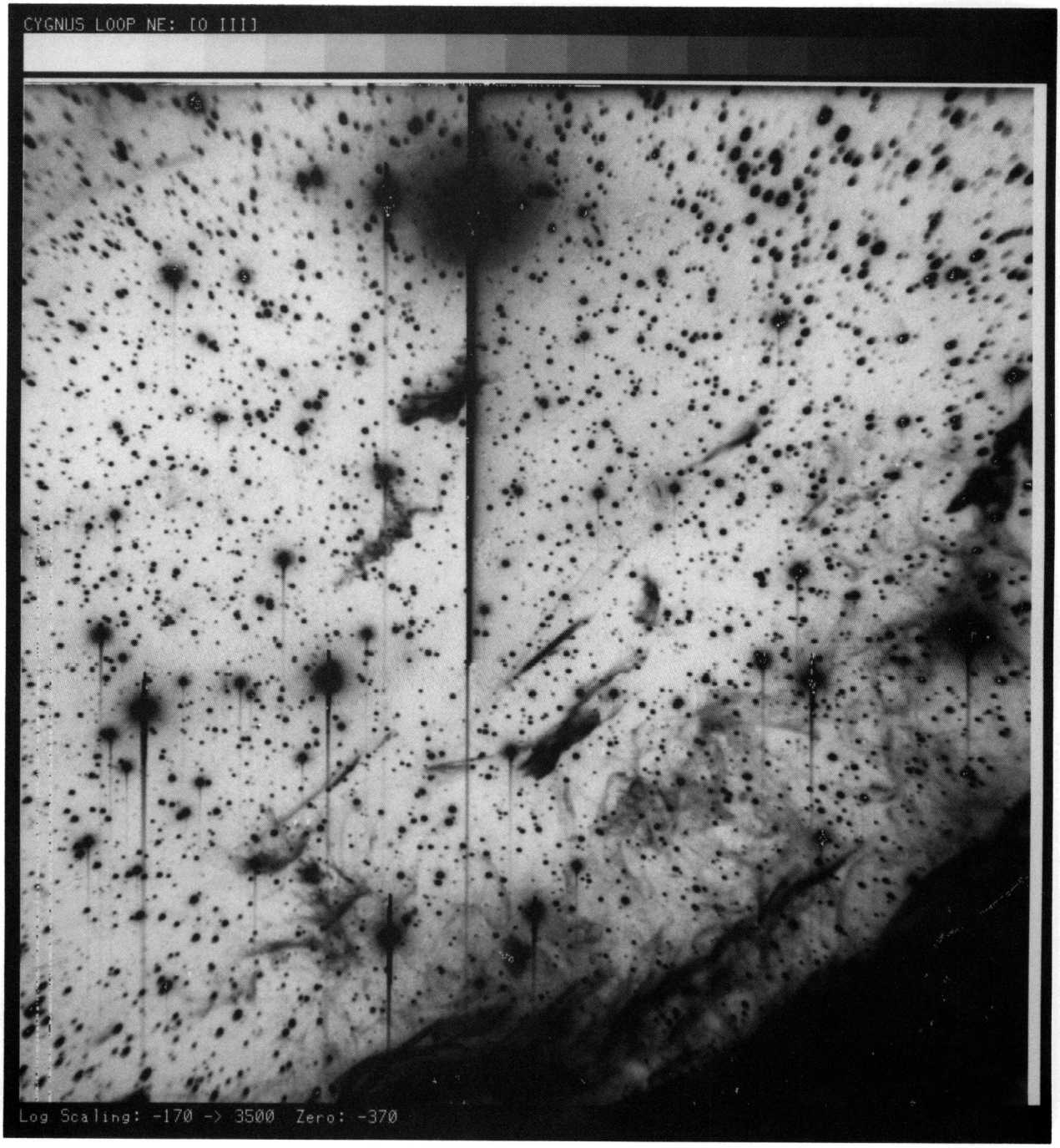

FIG. 1*b*

HESTER, RAYMOND, & BLAIR (see 420, 722)

[O III], is compromised by vertical and horizontal charge transfer effects from the bright star in the northern part of the frame.

The individual images were aligned with respect to each other using measured positions of a large grid of stars. The images were calibrated by reconstructing the object and sky apertures used by RBFG on our data. A check on the calibration was obtained from comparison with the MMT FOGS spectrum discussed in § 2.3. The detection thresholds in the final images (3 σ in a 3 × 3 pixel box) are 4.5×10^{-7} ergs cm^{-2} s^{-1} sr^{-1} for Hα and 1.7×10^{-7} ergs cm^{-2} s^{-1} sr^{-1} for [O III]. Positions of 16 stars in the field were obtained from the *HST* Guide Star Catalog and used in a least-squares fit to determine the mapping of the images onto absolute coordinates. The resulting fit, which has a rms residual of 1″, gave 1.″188 pixel^{-1} with the positive Y axis oriented 0.°4 east of north.

Of the Balmer-dominated emission in these images, only the two brightest filaments are visible on the POSS prints. We refer to the filament in the southeast corner of the field as filament 1 and the filament just to the south of the field center as filament 2.

A mosaic of the *Einstein* HRI data for this field was obtained from the *Einstein* archives. These data were discussed by Ku et al. (1984). The HRI data were resampled to match the optical field. The X-ray image is shown in Figure 2 (Plate 16). No data were available for the wedge in the northern portion of the frame. Intercomparison of the X-ray and visible data is facilitated by Figure 3 (Plate 17) which shows a color composite image of the field; [O III] is shown as green, Hα is shown as red, and the X-ray data are shown as blue.

2.2. *Echelle Spectroscopy*

2.2.1. *Observations and Instrumental Configuration*

High-resolution spectroscopy of several positions was obtained using the echelle spectrograph on the National Optical Astronomy Observatories 4 m telescope on Kitt Peak during two runs in 1986 September and 1988 September. The spectrograph was used in a long-slit mode, with the cross disperser replaced with a flat mirror. Order separation was accomplished using a narrow-band filter. The spectra were recorded on an 800 × 800 TI CCD. A 79 g mm^{-1} grating was used on both runs, giving a resolution of 5 km s^{-1} pixel^{-1}. On-chip binning (2 pixels in the slit dimenson by 1 pixel in the dispersion dimension) was used to reduce read noise contributions. The chip was preflashed before each exposure to reduce the effects of deferred charge.

During the 1986 September run, spectrograms of three positions were obtaining using a 200 μm slit, which gave an instrumental resolution of 20 km s^{-1}. Table 1 gives exposure data for the echelle data. Figure 4 (Plate 18) shows the positions of the echelle slits (along with apertures used for optical and UV spectrophotometry) overlaid onto the Hα and [O III] images. These positions included two pointings on and just to the southwest of filament 1, running parallel to the filament (E1 and E2, respectively), as well as a position running east–west across filament 2 (E2). These data appeared to confirm earlier suggestions that the narrow component of the Hα line profile was unexpectedly broad (RBFG; Treffers 1981), so an additional observation of filament 1 (E4) was obtained in 1988 September using a 100 μm slit, giving an instrumental resolution of 12 km s^{-1}. A spectrogram was also obtained in 1988 of the morphologically peculiar emission in the southwest part of the field imaged (E5).

TABLE 1

KPNO 4 m Echelle Observations

Position	α(1950)	δ(1950)	PA[a]	Date (UT)	Exposure (s)
E1	20^{h}53^{m}59^s.2	+31°45′07″	50°	1985 Sep 6	1800
E2	20 53 59.0	+31 45 07	50	1985 Sep 6	1800
E3	20 53 44.2	+31 47 12	90	1985 Sep 6	3600
E4	20 53 58.2	+31 45 23	42.5	1988 Sep 3	3600
E5	20 53 33.4	+31 45 20	90	1988 Sep 1	3000

[a] PA measured W of N.

2.2.2. *Data Reduction and Analysis*

The data were bias and preflash subtracted using stacked preflash frames and flattened against dome flats. Cosmic rays were removed from the frames using an iterative high-pass filter rejection and interpolation algorithm. Geometrical distortion corrections and wavelength linearization were achieved using fits to lines from a ThA comparison source. Figure 5 shows the 1988 spectrogram of filament 1 (E4) following sky subtraction using data from the ends of the slit, which did not fall on bright emission. Figure 6 shows the spectrogram of the morphologically peculiar emission at E5.

One-dimensional spectra were then extracted from the reduced spectrograms of the Balmer-dominated emission. Hα line profiles were fitted using nonlinear least-squares techniques assuming a linear baseline and a two-component Gaussian profile. Table 2 gives a list of the line widths and formal uncertainties for the narrow and broad components of the echelle spectra of Balmer-dominated emission. The spectrum at E1 is split into two sections corresponding to the northern and southern ends of filament 1. The spectrum at E3 is split into two sections corresponding to the northern and southern ends of filament 1. The spectrum at E3 is split into two sections as well. These correspond to the eastern portion of filament 2, which has little [O III] emission, and the western portion of filament 2, where the [O III] emission is significantly stronger. Where possible, spectra were measured both with and without sky subtraction, with very little effect on the measured width of the narrow component. Because the increased noise in the sky-subtracted spectra degraded the reliability of the fit to the broad component, we report widths taken from the unsubtracted spectra for all but the 100 μm slit spectrum at E4. All of the widths reported in Table 2 have had the instrumental resolution (12 km s^{-1} for the 100 μm slit and 200 km s^{-1} for the 200 μm slit) removed in quadrature from the measured widths.

To assess the reliability of a fit we began by estimating the deviance of the data as the rms residual of a linear fit to a line-free portion of the spectrum, and used this value to convert the rms residual of the Gaussian fit to a reduced χ^2. We then constructed a χ^2 surface in the $\Delta v_{\rm broad} - \Delta v_{\rm narrow}$ plane by recomputing the best fit and associated residuals while forcing the two widths to values on a grid. The contours of the resulting surface then formally denote regions of equal reliability for the fit. Figure 7 shows equal reliability contours for the fit to the spectrum at E4.

Figure 8*a* shows the extracted one-dimensional spectrum, together with the best fit and the individual components making up this fit. Also shown are the residuals to the fit.

PLATE 16

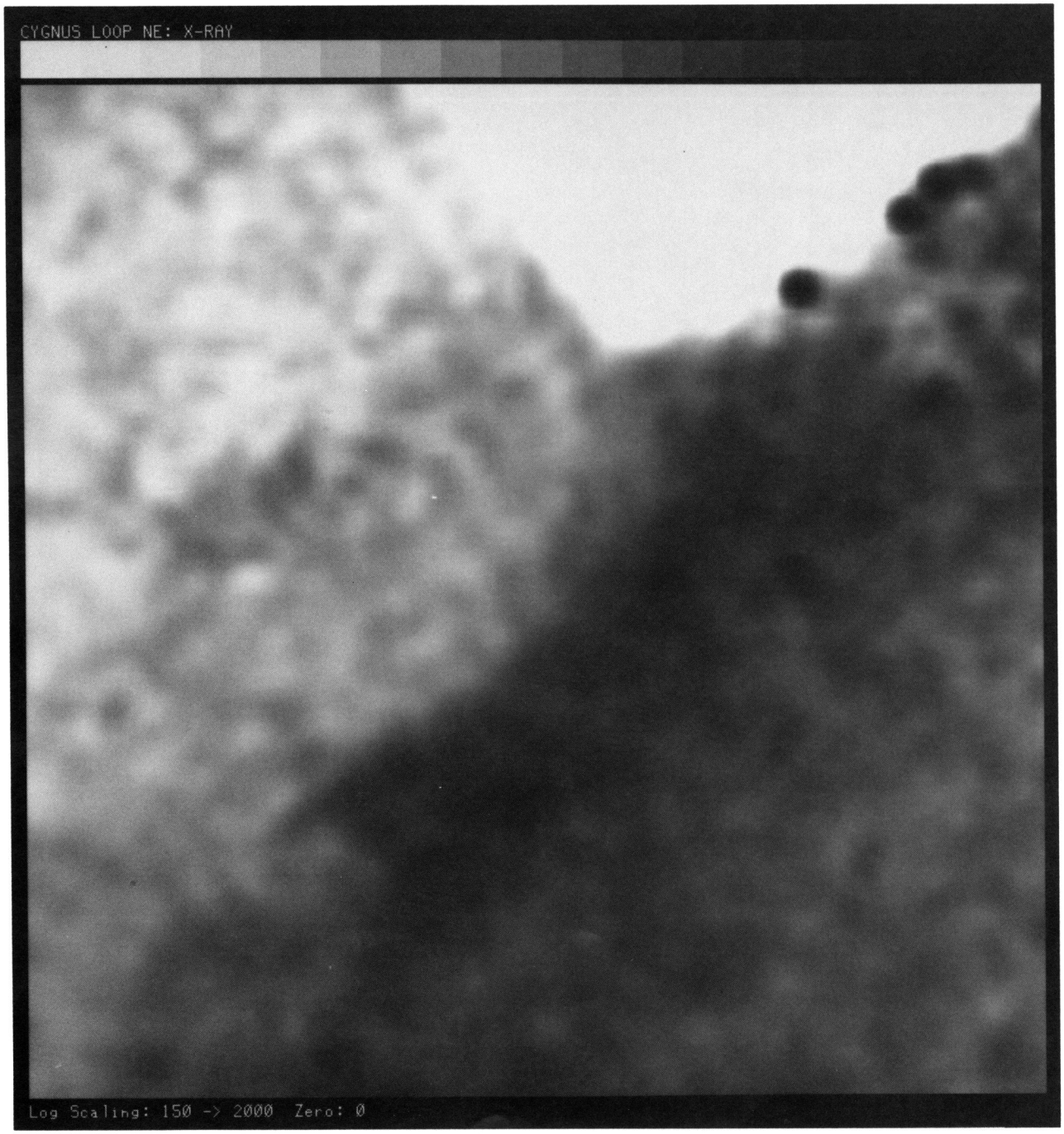

FIG. 2.—Soft X-ray image of the field shown in Fig. 1. The image is a composite of exposures taken with the *Einstein* High Resolution Imager. The missing wedge in the northern part of the frame is due to missing data. The data are displayed logarithmically.

HESTER, RAYMOND, & BLAIR (see 420, 723)

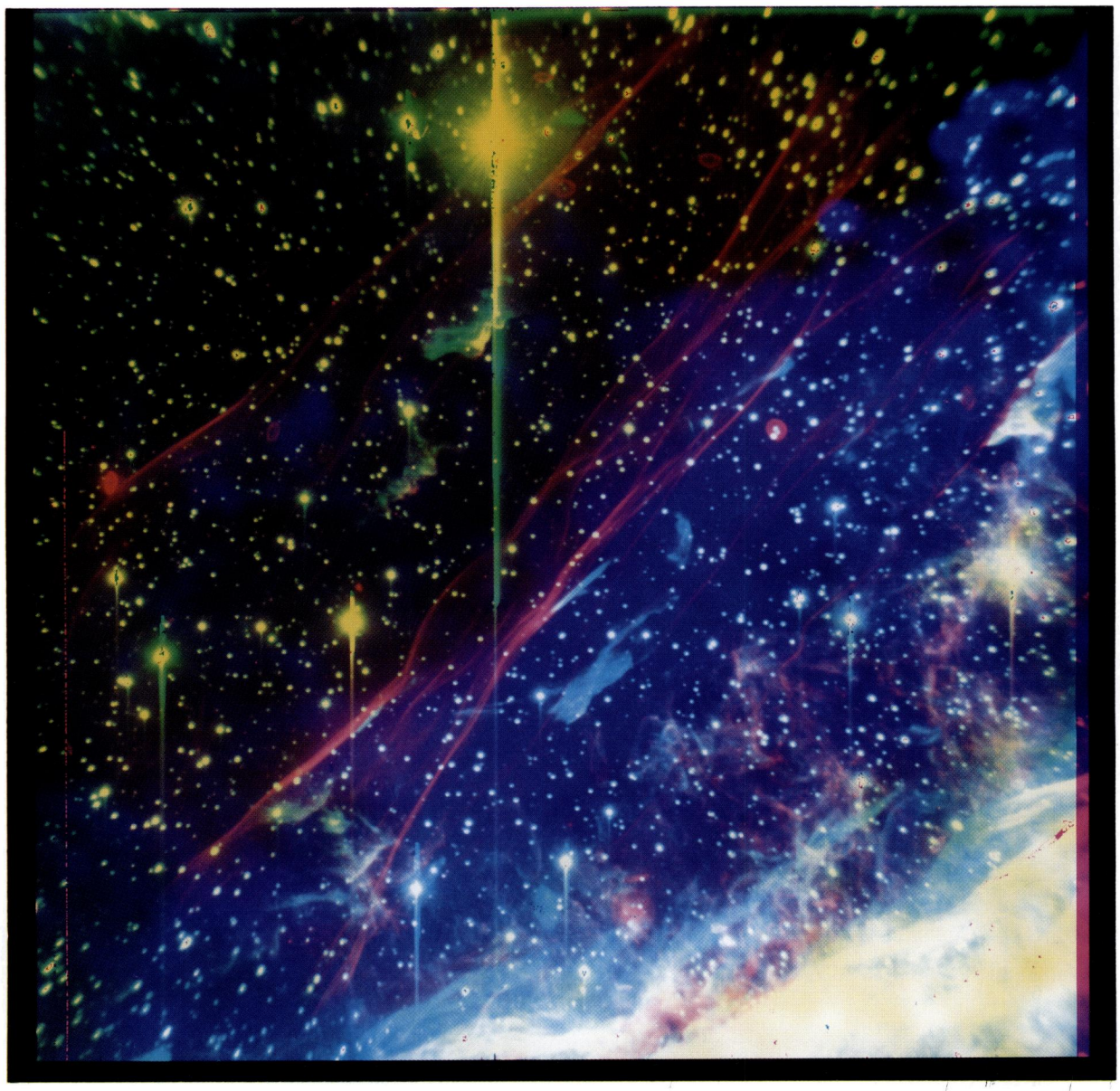

FIG. 3.—Color composite image of the field shown in Fig. 1. The Hα data are shown as red, the [O III] data are shown as green, and the X-ray data are shown as blue. The image shows, in particular, the relationship between the Hα filaments which show the current location of the blast wave, and the hot X-ray emitting gas which is trapped behind the shock.

HESTER, RAYMOND, & BLAIR (see 420, 723)

PLATE 18

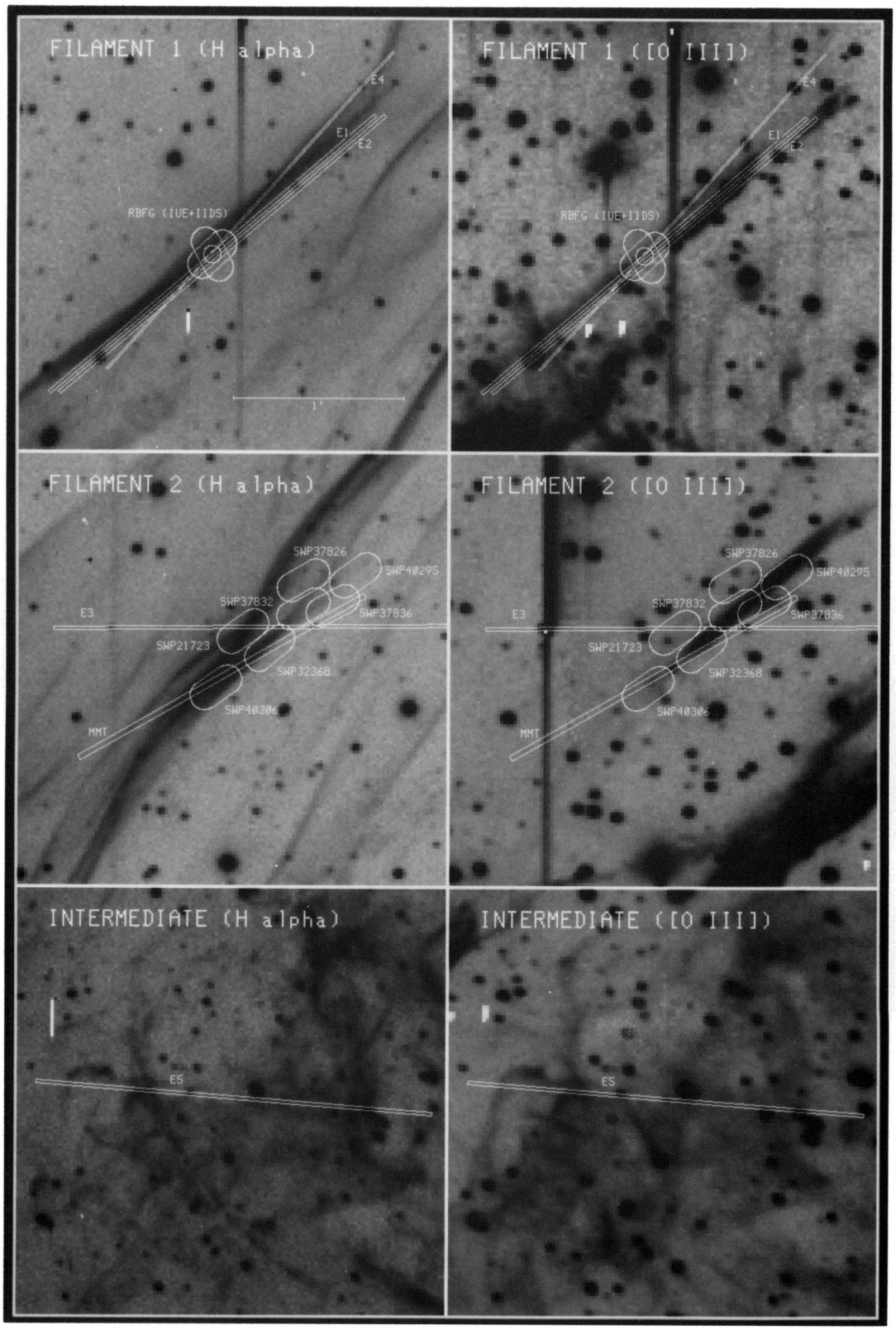

FIG. 4.—Positions of spectrograph slits and apertures. All figures are displayed at the same scale. For filament 1 the apertures displayed include the IIDS (*circle*) and *IUE* positions discussed by RBFG, and echelle positions E1, E2, and E4 presented in the current paper. For filament 2 the positions of six *IUE* apertures are shown, together with the slit position of the MMT FOGS spectrum and echelle position E3. The field of "intermediate" radiative emission shows echelle position E5. For echelle positions E1–E4, the central 150″ of the ~200″ slit is shown. For position E5 the central 140″ of the slit is shown.

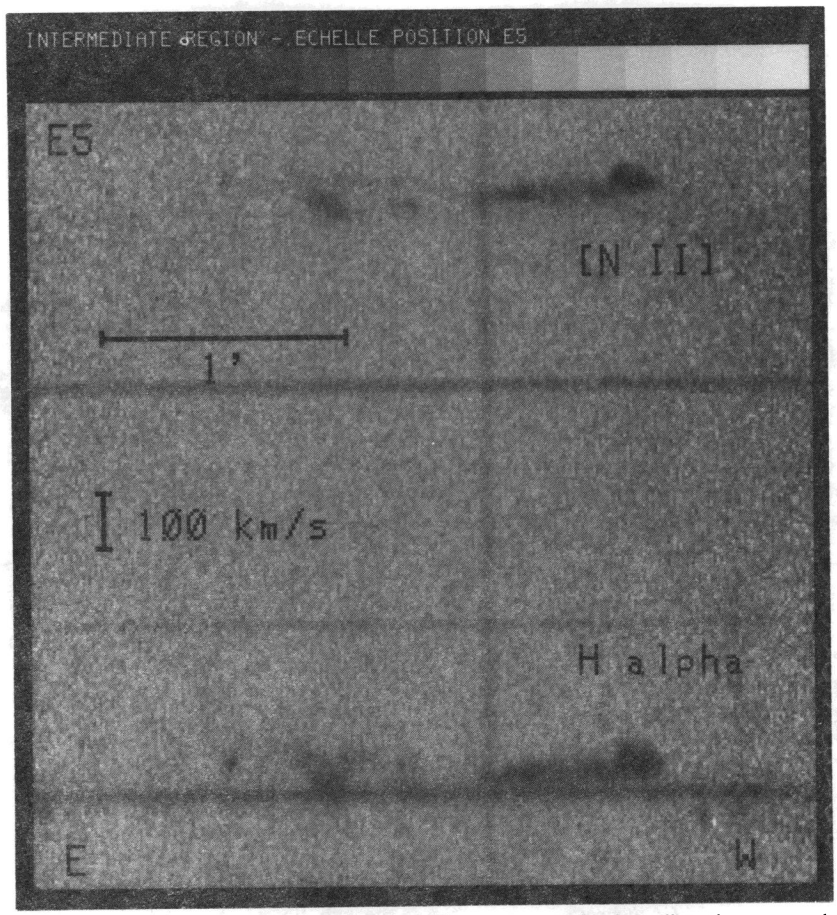

FIG. 5.—Echelle spectrogram of Hα emission from filament 1 along position E4. The spectrogram has been distortion corrected and placed on a linear wavelength scale, then sky-subtracted using emisson from the ends of the slit, which lie off the bright filament. The resolution of the spectrum, measured from night sky lines, is 12 km s^{-1}. The bars indicate the spatial and velocity scales.

Figure 8*b* shows the same spectrum with a fit in which the narrow component has been forced to a value at the 90% reliability contour. Direct examination of the residuals to the profile fits suggests that the formal uncertainties estimated above are conservative. The residuals in Figure 8*b* are clearly not random, but rather show a well-organized three-peaked structure characteristic of a systematic error in the model.

2.3. *Optical Spectrophotometry*

Low-dispersion spectra were obtained with the FOGS spectrograph on the Multiple Mirror Telescope using the aperture plate system designed by D. Fabricant. This device made it possible to obtain spectra of positions within a 2′ × 4′ field. Set star positions, as well as spectrograph entrance slits, are machined onto the aperture plate, so that the positioning is good to an arcsecond. The aperture plate made for these observations had a 2″ × 116″ slit at the center and two 58″ slits at positions chosen to cover fainter filaments. Because of the faintness of these positions and the vignetting of the MMT, the spectra from these secondary positions are of lower quality than the spectrum from the central slit and will not be discussed further. The position of the slit is shown in Figure 4.

TABLE 2

Hα LINE WIDTHS (km s^{-1})[a]

Position	Slit (μm)	Broad (68%)	Broad (90%)	Narrow (68%)	Narrow (90%)
Filament 1:					
E1 (NW end)	200	132 ± 14	134 ± 20	33 ± 2	33 ± 3
E1 (SE end)	...	122 ± 8	123 ± 11	30 ± 1	30 ± 2
E2	200	112 ± 26	117 ± 39	28 ± 3	28 ± 4
Filament 2:					
E3 (E end)	200	168 ± 12	166 ± 24	32 ± 2	32 ± 2
E3 (W end)	...	118 ± 38	129 ± 56	36 ± 6	35 ± 10
Filament 1:					
E4[b]	100	130 ± 10	130 ± 15	33 ± 2	33 ± 3

[a] After quadratic deconvolution with measured width of night sky line.

[b] Obtained during 1989 September. Instrumental resolution determined from sky lines = 12 km s^{-1}. All 200 μm slit observations had 20 km s^{-1} resolution.

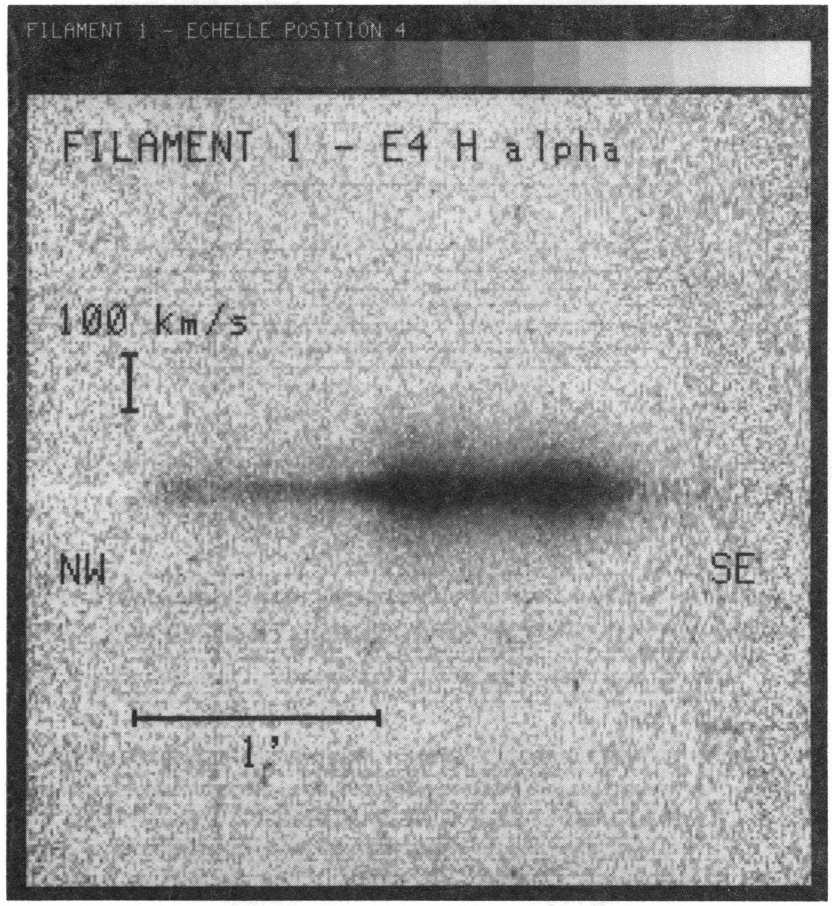

FIG. 6.—Echelle spectrogram showing emission from Hα and [N II] λ6584 along position E5, located in the "intermediate" region between the Balmer-dominated filaments and the bright northeast limb of the Cygnus Loop. The spectrum has been distortion-corrected and the wavelength scale linearized, but has not been sky-subtracted. The resolution of the spectrum is 20 km s^{-1}.

The alignment of the slit with the images was accurately determined by comparing the Hα and [O III] profiles along the slit with profiles extracted from the image data.

The data were recorded on a TI CCD and reduced in the standard way using IRAF. The spectra had good sensitivity over the 4500–7500 Å range and had a spectral resolution of 20 Å. Each pixel corresponds to 0".451 along the slit. Spectra were extracted in 10 pixel bands chosen to avoid stellar spectra and a bad column on the CCD. The measured line strengths in these 2" × 4".51 samples are given in Table 3.

We also obtained blue optical spectroscopy of the portion of filament 2 co-observed in the UV with SWP 21723 (see below). This observation was obtained on 1984 October 24 UT using the MMT and MMT (Reticon) spectrograph. Figure 4

TABLE 3

FLUXES ALONG MMT SLIT (10^{-16} ergs cm^{-2} s^{-1} in 4".51 × 2" section)

Sample	Position[a]	He II λ4686	Hβ λ4861	[O III] λ4959	[O III] λ5007	Hα 6563
1	−21"	1.41	1.44	1.20	5.04	6.48
2	−16	3.93	7.59	2.01	8.52	30.0
3	−11	7.35	23.2	2.07	6.54	78.0
4	−1	5.22	43.2	1.65	5.37	122.
5	4	6.06	47.4	2.64	7.29	138.
6	9	4.98	52.5	...	1.41	141.
7	14	5.16	39.9	...	1.56	104.
8	19	2.76	24.8	...	0.96	67.8
9	24	1.98	16.8	...	...	41.1
10	29	1.08	6.87	...	...	23.5
11	34	2.19	9.66	...	...	25.9
12	39	...	8.34	...	...	22.1
13	44	...	4.41	...	...	11.3
14	49	...	2.13	...	...	5.55

[a] Position measured from slit center, with positive numbers to the SE.

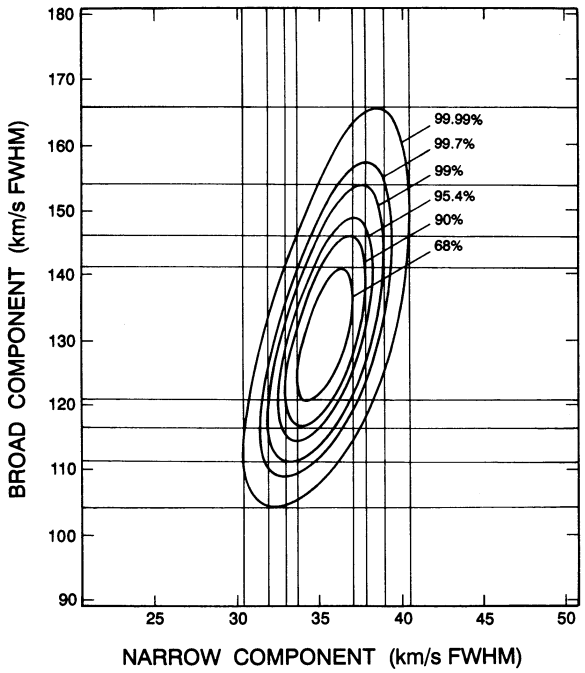

FIG. 7.—Contours showing formal confidence limits in a plane defined by the widths of the broad and narrow components for the fit to the Hα line profile for filament 1, taken from the sky-subtracted spectrum at position E4. The surface was determined by fixing the widths of the narrow and broad Gaussian components at each point on a grid covering the range of parameters shown, computing the best fit at that point varying all other parameters of the fit (line centers and amplitudes and the background level), then evaluating the reduced χ^2 using an estimate of the deviance obtained from the background. The vertical lines show the uncertainties in the width of the narrow component at the 68%, 90%, 99%, and 99.99% confidence levels. The horizontal lines show the uncertainties in the width of the broad component for these same levels.

shows the *IUE* aperture position, which was on the upper branch of filament 2 at the position where the E2 echelle slit cuts across the filament. A 2″ × 3″ aperture was placed on the filament at the center of the *IUE* aperture position for a total integration of 15 m. "Sky" background was sampled at positions 32″ east and west of the filament, in regions containing no bright emission (although very faint diffuse emission would have been present). An 800 line mm^{-1} grating was used in first order to provide coverage from 3250 Å to 5230 Å with less than 3 Å resolution. Standard star observations from the same night allowed the observation to be placed on a flux scale, although conditions were not photometric. The observed relative line intensities are shown in Table 4, as are reddening-corrected values in both flux units, and scaled to Hβ = 100. Scaling relative to the *IUE* data at this position was accomplished using our optical imagery to determine the relative optical fluxes in the apertures, as described in more detail in § 2.4.2.

2.4. *UV Spectrophotometry*

2.4.1. *New IUE Observations*

Ultraviolet spectra of five positions in the vicinity of filament 2 were obtained with the *IUE* satellite (Boggess et al. 1978) in the low dispersion mode. The positions and exposure times are listed in Table 5. Blind offsets were made from the 10th magnitude star used by RBFG, so the positions should be accurate to 1″–2″. These positions were mapped onto the optical images using the astrometric fit described above. The aperture positions are superposed on the Hα and [O III] images in Figure 4.

Line-by-line files of the *IUE* Guest Observer tapes were used to remove cosmic-ray events and extract spectra across the large aperture. Few changes in line ratios were seen between the central parts and ends of the spectra, and the highest signal-to-noise spectra were generally obtained when the central portion of the aperture was summed. Figure 9 shows the spectra obtained from the central 8 lines (8″.5) of each spectrum. In SWP 32368 and SWP 37836 the emission lines were centered several angstroms to the blue of the nominal wavelengths, indicating that the emission was concentrated in the northeast half of the aperture. This provides a check on the reliability of the positions shown in Figure 4.

Table 6 presents measured line strengths before and after correction for interstellar reddening using Seaton's (1979) reddening law, and assuming $E(B-V) = 0.08$ (Parker 1967). Where continuum was apparent in the spectrum the fluxes for the two-photon continuum were derived from the theoretical shape of the continuum and the flux in a 100 Å band centered at 1825 Å, a region free of emission lines and relatively free of major camera artifacts.

Line strengths for [O III] and Hα were obtained by superposing 20″ × 10″ apertures on the Hα and [O III] images at the locations of the *IUE* spectra. The local sky value for [O III]

TABLE 4

COMBINED UV/OPTICAL SPECTRUM OF FILAMENT 2
SWP 21723+MMT

Line	λ (Å)	F_λ^a	I_λ^b	$I/I_{H\beta}$
		Optical Spectrophotometry[c]		
[Ne V]	3426	6.0×10^{-15}	8.9×10^{-15}	17
[O II]	3727	5.5	7.8	15
He I + H	3889	5.4	7.6	14
Hδ	4102	8.3	11.6	22
Hγ	4340	13.6	18.6	36
He II	4686	5.4	7.2	14
Hβ	4861	39.8	52.5	100
[O III]	5007	3.8	5.0	10
		UV Spectrophotometry		
N V	1240	...	4.8×10^{-13}	915
C IV	1550	...	3.2	610
He II	1640	...	2.4	457
2 − γ	...	...	32.	6100

[a] Ergs cm^{-2} s^{-1}.
[b] Same units, corrected for interstellar extinction assuming $E(B-V) = 0.08$.
[c] Normalized to IUE aperture using optical imagery.

TABLE 5

IUE OBSERVATIONS OF FILAMENT 2

SWP	α(1950)	δ(1950)	PA[a]	Date (UT)	Exposure (minutes)
21723....	$20^h53^m44^s.81$	+31°47′10″.5	54°	1983 Dec 8	790
32368....	20 53 44.07	+31 47 04.5	49	1987 Nov 20	380
37826....	20 53 43.15	+31 47 28.5	59	1989 Dec 15	425
37832....	20 53 43.15	+31 47 18.5	60	1989 Dec 16	410
37836....	20 53 42.34	+31 47 19.5	60.5	1989 Dec 17	395
40295....	20 53 41.71	+31 47 30.5	54	1990 Dec 9	420
40306....	20 53 45.56	+31 46 50.5	55	1990 Dec 19	415

[a] PA measured W of N.

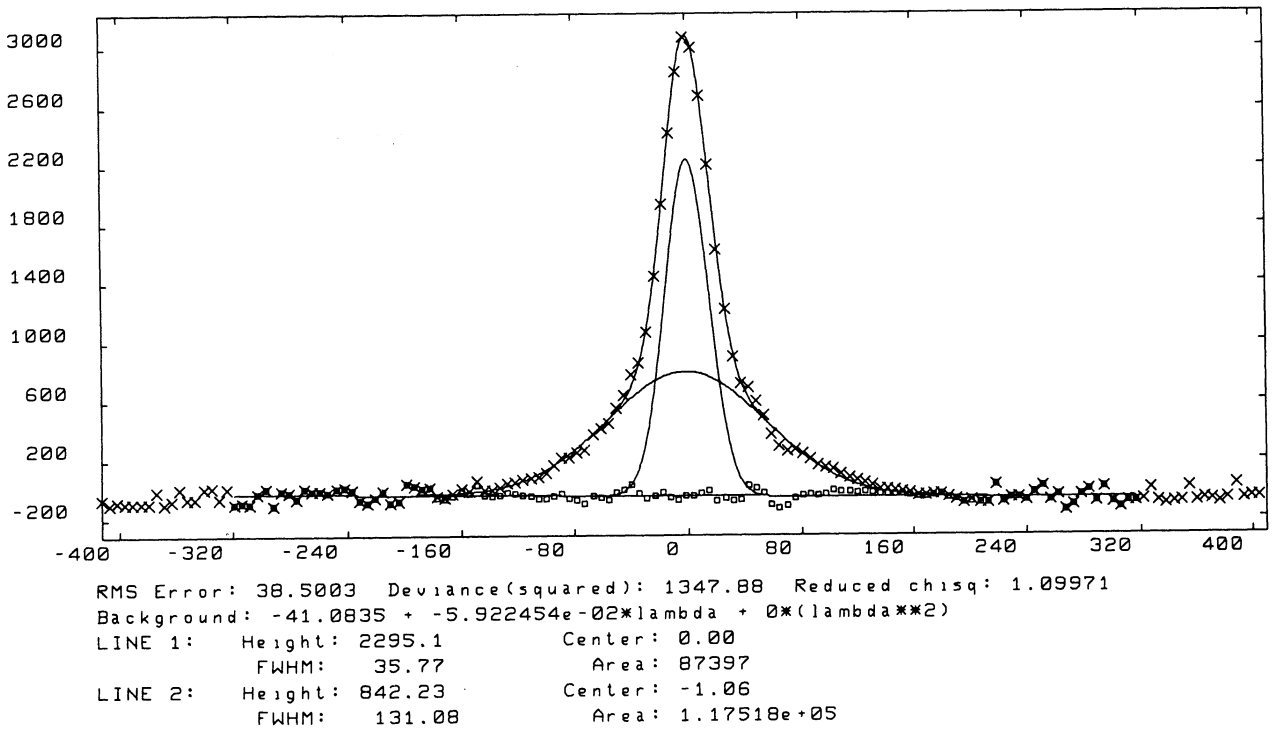

FIG. 8*a*

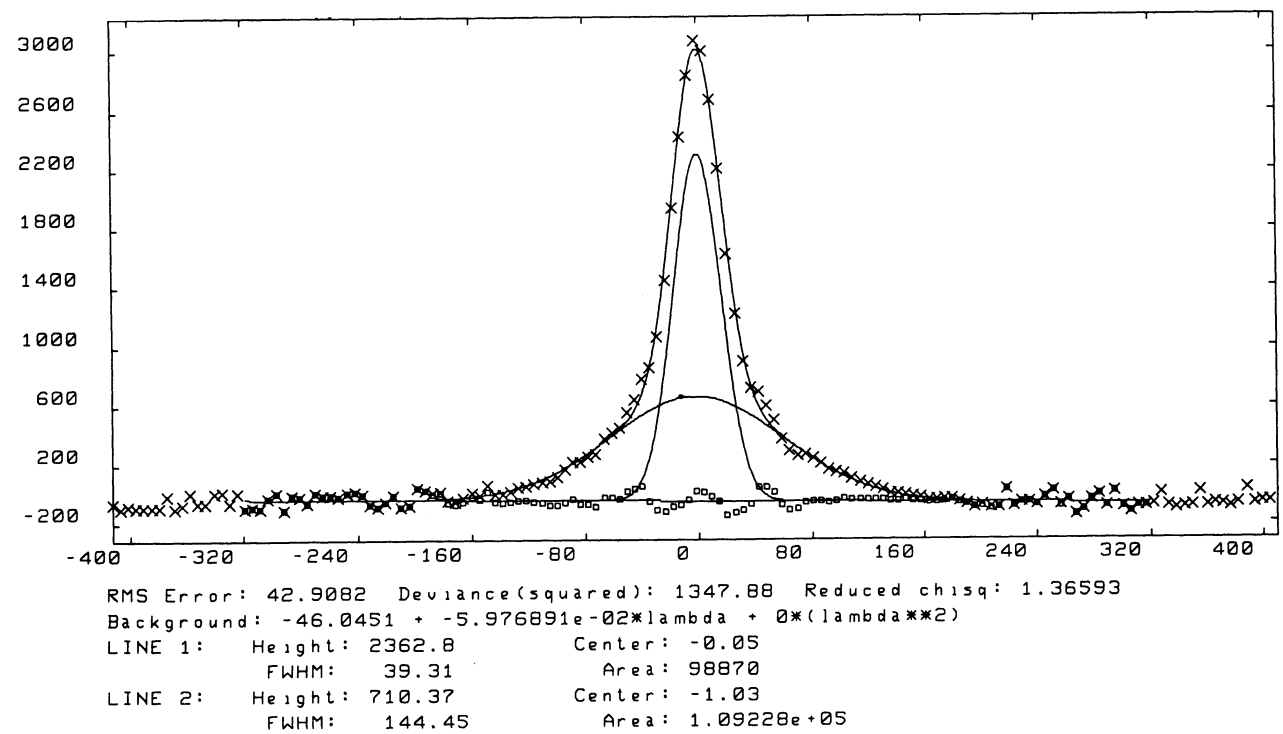

FIG. 8*b*

FIG. 8.—(*a*) The sky-subtracted Hα line profile extracted from the echelle spectrogram at position E4. The crosses show the data. The solid lines indicate the deconvolution of the line into two Gaussian profiles. The squares show the residuals to the fit. Flux units are arbitrary; velocities are in km s^{-1} relative to the best-fit center of the narrow component. The text gives the parameters of the fit. (*b*) A fit to the same data in which the widths of the broad and narrow components have been forced to a point on the 90% confidence contour. The fact that the errors to the fit are not randomly distributed suggests that the formal confidence computed from the fit is conservative.

TABLE 6

MEASURED LINE STRENGTHS[a]

LINE ID	SWP 21723			SWP 32368			SWP 37826			SWP 37832			SWP 37836			SWP 40295			SWP 40306			RBFG[c]
	F_λ	I_λ	I_λ/I_{CIV}	F_λ	I_λ	I_λ/I_{CIV}	F_λ	I_λ	I_λ/I_{CIV}	F_λ	I_λ	I_λ/I_{CIV}	F_λ	I_λ	I_λ/I_{CIV}	F_λ	I_λ	I_λ/I_{CIV}	F_λ	I_λ	I_λ/I_{CIV}	I_λ/I_{CIV}
N v λ1240.....	2.34	4.80	150	0.91	1.87	107	0.35	0.72	79	0.78	1.60	86	0.61	1.25	97	1.79	3.67	139	1.38	2.38	195	140
O IV] λ1400....	...	...	...	0.45	0.84	48	<0.13	<0.24	<26	0.56	1.05	56	0.63	1.18	91	0.95	1.78	67	...	...	...	<39
N IV] λ1486....	...	...	...	0.27	0.49	28	<0.13	<0.24	<26	0.41	0.75	40	0.52	0.95	74	...	...	...	...	...	...	...
C IV λ1550	1.77	3.20	100	0.96	1.74	100	0.50	0.91	100	1.03	1.86	100	0.71	1.29	100	1.46	2.64	100	0.80	1.45	100	100
He II λ1640	1.35	2.40	76	0.52	0.93	53	<0.13	<0.23	<25	0.10	0.18	10	<0.15	<0.27	<21	0.17	0.30	11	0.69	1.23	86	67
C III] λ1909	...	...	...	0.20	0.36	21	0.10	0.18	20	<0.10	<0.18	<10	0.19	0.34	26	...	...	...	...	...	...	<13
2 − γ	17.5	32	1000	<5.	<9.	<520	10.	18.	1980	<7.	<13.	<700	<5.	<9.	<700	...	...	...	...	...	...	1223
[O III] λ5007[b]...	...	0.032	1.0	...	0.25	14	...	0.037	4.1	...	0.48	26	...	0.31	24	...	0.38	14	...	0.053	3.7	2.5
Hα λ6563[b]	...	1.59	50	...	0.78	45	...	0.52	57	...	0.42	23	...	0.17	13	...	0.15	5.7	...	1.81	125	60

[a] F_λ is the observed flux in units of 10^{-13} ergs cm^{-2} s^{-1}. I_λ is the dereddened flux in the same units. $I_\lambda/\lambda_{C\,IV}$ is normalized to 100.

[b] Optical fluxes extracted from CCD images using a 10″ × 20″ box to approximate the *IUE* aperture.

[c] Average of positions from RBFG.

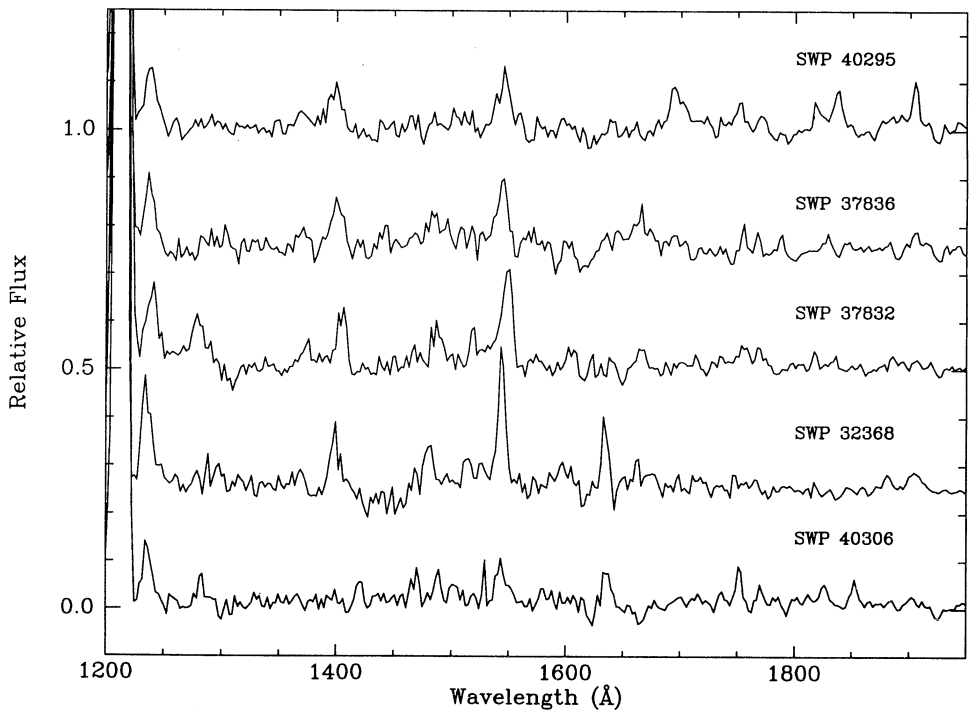

FIG. 9.—*IUE* spectra for the five positions along the length of filament 2. The spectra run from SWP 40295 at the northwest (strong [O III]) end of the filament of SWP 40306 at the southeast (strong Hα) end of the filament.

varies significantly across this region due to poor horizontal charge transfer from the bright star to the northeast of filament 2, so the [O III] line strengths for positions with [O III] $< 0.2 \times 10^{-13}$ ergs cm^{-2} s^{-1} are uncertain by up to a factor of 2. The *IUE* and optical spectra were normalized assuming a solid angle for the *IUE* aperture of 200 arcsec^2 (Panek 1982).

2.4.2. *Renormalization of RBFG UV and Optical Spectrophotometry*

Both the optical and *IUE* apertures used by RBFG were reconstructed on our optical images. The ratio of the Hα flux in the *IUE* aperture to the Hα flux in the optical aperture was 0.6 and 0.8 for the *IUE* apertures across and along the filament, respectively. The [O III]/Hβ ratio in the three apertures was remarkably constant—0.12, 0.14, and 0.14 for the *IUE* aperture across the filament, the *IUE* aperture along the filament, and the optical aperture, respectively. The similarity of these numbers suggests that the errors in the composite UV/optical spectrum due to true variation in the spectrum among the slits are small. These ratios were then used to renormalize the optical and UV spectrophotometry presented by RBFG. Table 7 gives the resulting composite UV/optical spectrum for this position. Also given in the table are line strengths for this position obtained from FI, including measurements of [N II] and [S II]. Again, the similarity of the He II λ4686 and [O III] λ5007 line strengths indicates that the spectral match between the different apertures is good.

3. MODEL CALCULATIONS

To facilitate interpretation of our spectroscopy and spectrophotometry, we computed models of the UV and optical emission behind nonradiative and partially radiative shocks. We present two types of models. Detailed kinetic models for H and He very close to the shock front were designed to compute line profiles, conversion efficiences of Lyβ photons to Hα, and precursor heating by broad component neutrals overtaking the shock. Global models which include the ionization and excitation of abundant elements through sulfur predicted the relative emission line intensities.

TABLE 7

COMBINED UV/OPTICAL SPECTRUM FROM RBFG AND FI[a]

λ (Å)	RBFG Values	FI values
Optical Spectrophotometry		
[Ne V] 3426	100	...
[O II] 3727	28	...
He I + H 3889	21	...
Hδ	31	...
Hγ	53	...
He II 4686	24	22
Hβ 4861	100	100
[O III] 5007	14	14
Hα	...	277
[N II] 6584	...	5
[S II] 6717 + 6731	...	5
UV Spectrophotometry[b]		
N V 1240	814	...
Si IV/O IV 1400	<140	...
C IV 1550	514	...
He II 1640	379	...
[C III] 1909	<70	...
2 − γ	6300	...

[a] Fluxes relative to Hβ = 100.

[b] Average of two positions, normalized to optical data using weighting obtained from optical imagery.

3.1. *Kinetic Models*

The kinetic model parameters are shock velocity, preshock density and ionization state, preshock electron and ion temperatures, and an efficiency for electron-ion temperature equilibrium by plasma turbulence. The last parameter ranges between 0, if the electrons are heated by Coulomb collisions alone, and 1 if $T_e = T_i$ everywhere. Ionization, excitation, and charge transfer rate coefficients from Smith et al. (1983a) and the Coulomb rate for electron-ion equilibrium from Spitzer (1978) are used to compute the ion and electron temperatures, the hydrogen and helium ionization states, and the broad and narrow component neutral hydrogen densities as functions of position behind the shock. Figure 10 shows the results of these calculations for a 170 km s^{-1} model with rapid equilibration and a 140 km s^{-1} model with Coulomb equilibrium.

The Balmer lines of H and He^+ are computed by a Monte Carlo simulation similar to that described by Smith et al. (1993a, b). Most of the excitations to the $n = 3$ states result in Lyβ photons. Each time a Lyβ photon scatters it has a 12% probability of converting to Hα plus a two-photon pair. The intensities and profiles of Hα and the analogous He II λ1640 line thus depend on the optical depths in the H and He^+ Lyβ lines. Given the temperatures and densities in the flow, the code computes the absorption line profiles at each position behind the shock. Lyβ photons are then emitted in proportion to the local emissivity in random directions with frequencies randomly distributed over the local line profile. Each photon is followed until it escapes from the grid or is converted to Hα. The converted photons are added to the profile of Hα which came from excitations to the 3*s* and 3*d* levels. The main results of these simulations are: (1) 70%–75% of the $n = 3$ excitations in the hydrogen narrow component and 30%–37% of the broad component excitations yield Hα photons, (2) only 3%–7% of the He II Lyβ photons convert to λ 1640, (3) Gaussian fits to the simulated Hα line profiles yield line widths the same as the original thermal widths of the emitting gas to within a few km s^{-1}, but the narrow component is made narrower by 1–2 km s^{-1} by more efficient conversion of Lyβ at line center.

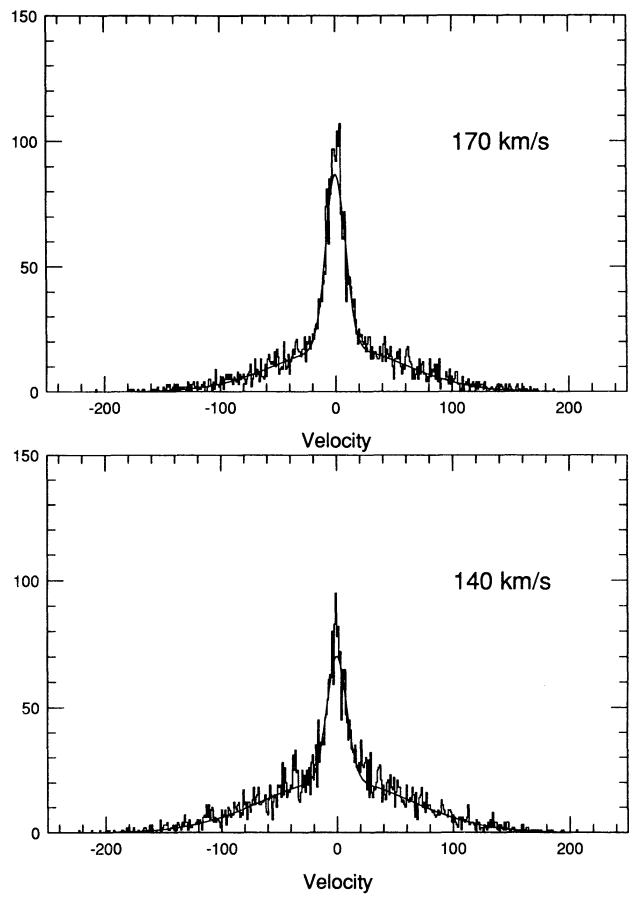

FIG. 10.—Models showing calculations of Hα line profiles for a 170 km s^{-1} shock with instantaneous postshock equilibrium of T_i and T_e, and for a 140 km s^{-1} shock with Coulomb equilibration. The widths of the broad components are the same in both cases.

The densities and temperatures computed in the first part of the simulation are also used to explore an interesting type of precursor heating. The broad component neutrals share the kinetic temperature and bulk velocity of the shocked ions. The postshock gas moves away from the shock at $v_s/4$, and the mean thermal velocity is a fair fraction of v_s (depending on the fraction of energy shared with the electrons), so that many of the neutrals are capable of overtaking the shock. To do so they must survive the transit without charge transfer or ionization, however, and only a few percent reach the shock to move ahead and deposit their energy in the preshock gas. The temperature of the precursor can be computed assuming that charge transfer leads to efficient heating of the neutrals and ions. The thickness of the precursor is small enough that radiative cooling can be ignored, but the ion-electron equilibration time at the low temperatures is comparable to the charge transfer time, and some of the heat will be shared with the electrons. The temperature of the precursor increases with increasing preshock neutral fraction and is higher for the case of Coulomb equilibrium than for rapid equilibrium. For a preshock neutral fraction of 0.8 and Coulomb equilibration, the precursor temperature for a 180 km s^{-1} shock could exceed 50,000 K. For a preshock neutral fraction of 0.3 and rapid equilibration, the preshock temperature could reach only about 4000 K. These temperatures are upper limits, however, in that much of the energy deposited in the precursor ions is advected back to the shock before it can be shared with the neutrals.

3.2. *Global Models*

The global models are basically similar to those of Raymond et al. (1988) and Long et al. (1992). We assume (for the time being) a steady flow behind a shock moving at constant velocity through a constant density medium. A computer code based on the analysis of Cox (1972a) follows the ionization state, radiative cooling, and emission line emissivities of the shocked gas. The code of Raymond (1979) with updated atomic rates as described by Cox & Raymond (1985) has been modified to allow an arbitrary partition of thermal energy between the electrons and the ions in the shocked gas. While the earlier models assumed equal ion and electron temperatures throughout the flow, both theoretical (Cargill & Papadopoulos 1988) and observational work (Smith et al. 1993a) suggest that only a small portion of the kinetic energy is transferred from ions to electrons at the shock front. Coulomb collisions will eventually equilibrate the electrons and ions, but much of the optical emission from a nonradiative shock may occur while $T_e \ll T_i$. The code includes Coulomb collisions in the equations for electron and ion thermal energies (Spitzer

1978). The applicability of this to the Cygnus Loop is discussed below (§ 4.6.2).

The basic shock model parameters are velocity (v_s), preshock density, transverse magnetic field and ionization state (n_0, B_0, and X_0), and elemental abundances. We assume only Coulomb equilibration of electron and ion temperatures. For the appropriate range of densities and field strengths, the spectrum is totally intensitive to the magnetic field and all the emission line intensities simply scale linearly with preshock density. The preshock ionization state is determined by the ionizing radiation from the shocked gas, which depends on the shock velocity and column density of gas which the shock has swept up. We will take the preshock ionization as a free parameter which can be estimated from an observed spectrum by the methods described by Cox & Raymond (1985). Elemental abundances are somewhat problematic. Just behind the shock front the abundances are depleted because neither sputtering nor grain-grain collisions will have had time to liberate elements such as carbon, silicon, or iron from refractory grains. Farther back in the cooling zone, though, the gas-phase abundances of these elements will increase as most of the grains are destroyed (Seab & Shull 1983). Long et al. (1992) found that, while normal C abundances were adequate to account for a Hopkins Ultraviolet telescope (HUT) spectrum of a radiative shock in the Cygnus Loop, depleted C abundances were required to match their spectrum at the nonradiative position. We assume the same abundances as those used by RBFG based on modest depletion in the diffuse interstellar medium (ISM): He = 10.93, C = 8.22, N = 7.96, O = 8.82, Ne = 7.96, Mg = 7.22, Si = 7.30, and S = 7.20. We have no observed Mg or Si lines, and they contribute so little to the total cooling that their abundances are unimportant. The models assume 30% neutral preshock H and He.

Figure 11 shows the accumulated emission line strengths for a number of visible and UV emission lines versus column depth swept up by the shock for a model of a 180 km s^{-1} shock. The figure demonstrates the sensitivity of shock spectrum to accumulated column density. Note, for example, that while emission from lines such as N v, C iv, and He ii are near their peak when the shock has swept up only a few times 10^{16} cm^{-2}, lines such as [O iii] and C iii do not become strong until the column depth exceeds 5×10^{17} cm^{-2}. The principal qualitative differences between this model and a model of a 140 km s^{-1} shock are (1) the high-ionization N v line is about a factor of 10 weaker in the 140 km s^{-1} model, and (2) the lower ionization lines such as [O iii] begin to turn on at a column depth of about 1.5×10^{17} cm^{-2}.

A major weakness of these models is the assumption that the flow bears some resemblance to a portion of a steady radiative shock flow. Several theoretical investigations have shown that shocks in the 150–200 km s^{-1} range are very unstable and subject to the formation secondary shocks (Innes, Giddings, & Falle 1986; Gaetz, Edgar, & Chevalier 1988; Innes 1992), and there is some observational evidence for thermally unstable cooling in the Vela SNR (Raymond, Wallerstein, & Balick 1991). We can get away with the steady approximation in this case largely because the cooling has not progressed far enough for the instability to drastically affect the structure. The existence of Hα from neutrals passing through the shock demonstrates that only a modest portion of the thermal energy has been radiated away, and the lack of low-excitation lines shows that no significant fraction of the gas has reached the low-temperature regime where the secondary shocks form in the numerical simulations. The largest difference between the models and calculations incorporating thermal instability is a nearly constant pressure cooling in our models and nearly constant density in the most unstable case. This leads to a smaller amount of radiation (3/2 kT per particle instead of 5/2 kT), a slightly more extreme departure from ionization equilibrium, and a slightly larger swept-up column density required to reach a given temperature.

A more severe problem may be the assumption that the

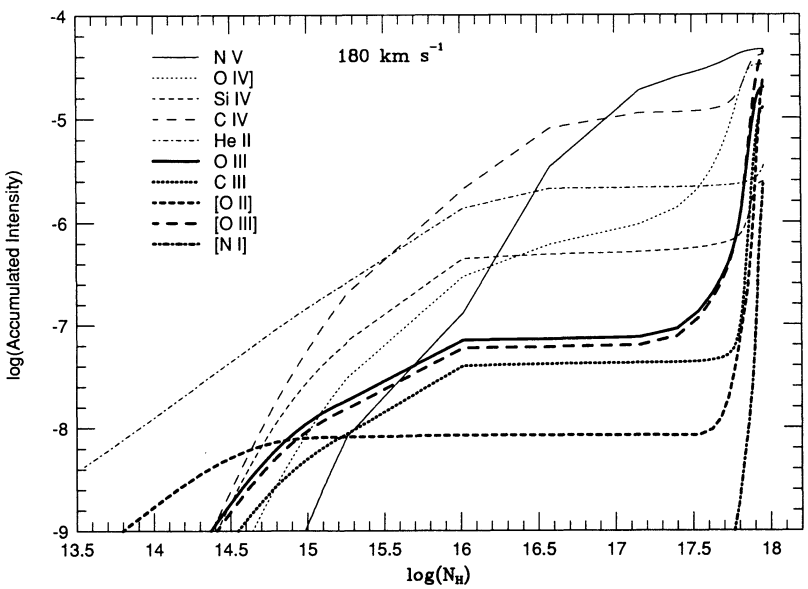

FIG. 11.—Accululated emission line strengths for a number of visible and UV emission lines vs. column depth swept up by the shock for a model of a 180 km s^{-1} shock with a 30% preshock neutral fraction. The figure demonstrates the sensitivity of shock spectrum to accumulated column density. Note, for example, that while emission from lines such as N v, C iv, and He ii are near their peak when the shock has swept up only a few times 10^{16} cm^{-2}, lines such as [O iii] and C iii do not become strong until the column depth exceeds 5×10^{17} cm^{-2}.

shock velocity and preshock density remain constant through the region producing the emission we observe. Possible implications of this for interpretation of the observed spectra are discussed in § 4.4.2.

4. RESULTS AND DISCUSSION

4.1. *Overview*

The optical and X-ray images of the northeast Cygnus Loop show that the Balmer-dominated filaments trace the shock front that forms the boundary of the SNR, and behind which is confined the hot X-ray emitting gas in the interior of the remnant. The morphology of the Balmer-dominated shocks in this region is extremely smooth, especially in comparison with the more irregular structure characteristic of radiative shocks elsewhere in the remnant. This smooth morphology requires that the preshock medium be quite homogeneous throughout this region.

The localized strengthening of forbidden line emission, specifically [O III], traces positions where the shock is undergoing a transition from a nonradiative or adiabatic shock to a radiative shock in which cooling is dynamically important. In the northeast Cygnus Loop this transition is visible in three different contexts. Initially, there are a number of locations (~ 5) where the shock has encountered localized regions of higher density in the ISM. These are apparent as regions of strong and much more irregular [O III] emission. Second, there are several locations where smooth [O III] filaments tie into the network of "regular" Hα filaments, tracing locations where gas behind the "undisturbed" blast wave is beginning to cool. Finally there is a zone of irregular structure, located between the strongly Balmer-dominated filaments and the bright radiative northeast limb, in which conditions must in some sense be intermediate between these two regions.

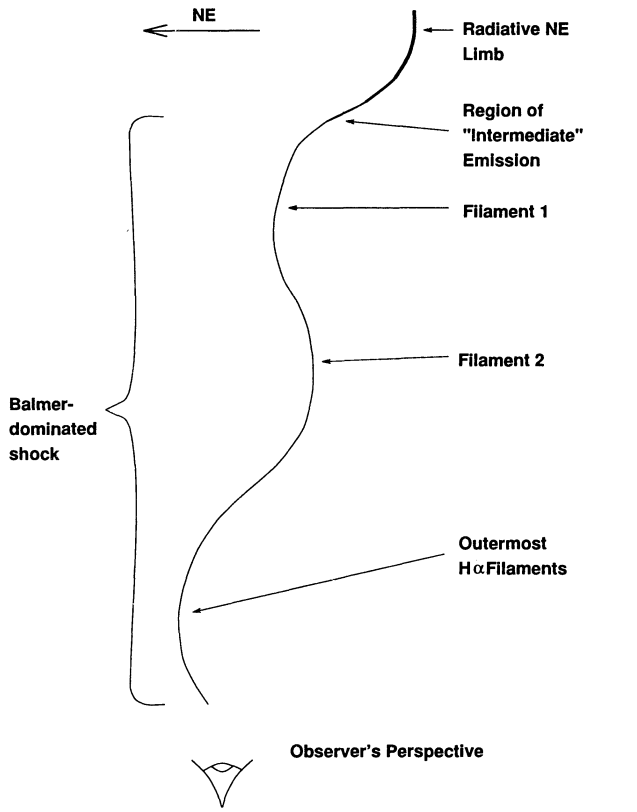

FIG. 12.—Sketch showing the geometry of the shock front in the field studied. The interior of the SNR is to the right, and northeast is to the left. There are four locations where the gross geometry of the shock front is tangential to the line of sight. These locations give rise to the three main lines of nonradiative shocks, as well as the bright radiative northeast limb of the Cygnus Loop.

4.2. *The Smooth Filamentary Emission*

The Hα image (Fig. 1*a*) shows that the region is filled with very smooth filamentary emission embedded within faint diffuse emission. It is clear from the morphology that the Hα emission arises in a gently rippled sheet, as discussed by Hester (1987). Filaments are locations where the shock is seen in tangency, while diffuse emission arises from locations where the shock is seen more nearly face-on. The smoothness of the Hα emission indicates that the preshock medium is remarkably homogeneous throughout the region and demonstrates the overall continuity of the structure. Specifically, it seems very unlikely that the preshock medium is composed of many small cloudlets, as suggested by FI.

There are three prominent, continuous lines of Hα filaments stretching from southeast to northwest across the field. The outermost of these traces the outer edge of the X-ray emission. The two lines of filaments crossing through the center of the field include filament 1 and filament 2. These two lines of filaments bound a strip in which the diffuse Hα emission is significantly brighter than elsewhere in the field. The relative brightness of the diffuse Hα emission in the three regions defined by these lines of filaments and the continuity of these structures indicate that the overall geometry of the region is as shown in Figure 12. From the perspective of the observer the sheet appears to extend from the bright radiative emission in the southwest corner of the field to the second line of nonradiative filaments, double back and again reach tangency at the line of filaments 1′–2′ to the southwest, and from there extend to the outermost tangency $\sim 7'$ to the northeast. Superposed on this structure are smaller ripples in the shock front which give rise to the many more localized filaments (i.e., shock tangencies) throughout the field. The conclusion is that we are looking at a single large-scale shock front which cleanly marks the boundary between the interior of the SNR and the surrounding medium.

The more prominent Balmer-dominated filaments can also be seen faintly in the [O III] image. The [O III]/Hβ ratio has a fairly uniform value of ~ 0.1 for filaments which are bright enough to be seen in [O III]. In addition, there are two [O III] filaments near Hα filaments 1 and 2 which are associated with the smooth filamentary emission but which are significantly brighter than average in [O III]. We will argue below that these mark locations where the shock is undergoing a transition from an adiabatic shock to a radiative shock. It is perhaps not surprising that the brightest, and therefore best studied, Hα filaments in this region are atypical in that they lie in close proximity to regions of bright [O III]. The optical spectrum presented by RBFG, for example, has [O III]/H$\beta \sim 50\%$ higher than average for Balmer-dominated emission in the field. On the basis of this criterion, the spectrum of a position along filament 2 presented in Table 4 is more typical of Balmer-dominated filaments in the region.

Throughout the field regions of bright X-ray emission are sharply bounded by Balmer-dominated filaments. This includes the line of filaments in the northeast corner of the field

which bound the X-ray "halo" discussed by Ku et al. (1984), showing that this halo is simply thermal emission from hot gas in the interior of the remnant. The X-ray emission behind the two lines of filaments across the center of the field is sharply limb-brightened, indicating that the X-ray emission is much brighter in a zone about 1′ ($\lesssim 10^{18}$ cm) thick behind the shock.

4.3. *Viewing Angle and Preshock Density*

A fundamental difficulty in interpreting shock spectra is the uncertainty in the projection angle at which the shock is being viewed. Derived quantities such as the face-on surface brightness of the shock, the preshock density, and the pressure depend on this angle. Fortunately, our data provide us with a number of constraints on the viewing angle or aspect ratio of the shock in our field.

Initially, from the ratio of the brightness of the filaments to the brightness of the diffuse emission, we estimate that the aspect ratios of these two components typically differ by a factor of 5–10. The brightest filaments are ~ 40 times less face-on than the surrounding diffuse emission. This is consistent with the long smooth filament morphology observed; given the regularity of the observed morphology, it is expected that in some locations the shock will remain nearly tangent to the observer along a significant line of sight.

None of the echelle spectra shows any significant offset between the center of the broad components and the center of the narrow component, as would be expected if the shock were viewed significantly face-on. The position southwest of filament 1 (E2) was chosen specifically to look for such an offset, but even in this case the formal best-fit offset between the components is only 0.5 km s^{-1}. Interpretation of this result is complicated by the fact that there are three shock crossings along this line of sight (Fig. 12). However, while multiple shock crossings might yield a composite profile centered at 0 velocity, the width of the component would be significantly broadened. Two shock crossing at an aspect ratio of 10:1 would broaden the apparent width of the line by $\sim 20\%$ of the shock velocity. Formally, the broad component at E2 is actually narrower than that at E1 (see Table 2). A 20% broadening of E2 with respect to E1 is about the limit of what is allowed within the 90% confidence limits of the fits to the line profiles. We conclude that on average the line-of-sight velocity at any shock crossing at E2 is less than 10% of the shock velocity, requiring that the shock is viewed no more than $\sim 6°$ from tangency at this location.

This result can be used to infer a value for the preshock density. The observed surface brightness of a shock is

$$I_{\rm obs} = \frac{h\nu}{4\pi} A \left(\frac{N_{\rm H\alpha}}{N_{\rm H0}}\right) f({\rm H0}) n_0 v_s ,$$

where A is the aspect ratio due to the viewing angle of the shock, $N_{\rm H\alpha}/N_{\rm H0}$ is the number of Hα photons produced per neutral H atom passing through the shock, and f(H0) is the preshock neutral fraction. The surface brightness of the diffuse Hα emission to the southwest of filament 1 (the brightest diffuse emission observed) is 6×10^{-6} ergs cm^{-2} s^{-1} sr^{-1}. Assuming three shock crossings, this is an average surface brightness of 2×10^{-6} ergs cm^{-2} s^{-1} sr^{-1} in each shock crossing. Assuming an aspect ratio greater than 5 (a factor of 2 more conservative than above) and using values of $N_{\rm H\alpha}/N_{\rm H0} = 0.1$ (Cox & Raymond 1985), f(H0) = 0.3 (RBFG), and $v_s = 180$ km s^{-1} gives an estimate for the preshock density of $n_0 < 3$ cm^{-3} ($n_0 < 1.5$ cm^{-3} using the less conservative $A > 10$). This is consistent with the value of 2 cm^{-3} inferred by RBFG, but somewhat lower than the range of densities derived by Long et al. (1992).

4.4. *The Nonradiative/Radiative Transition along Filament 2*

Figure 13 shows the relationship between Hα and [O III] along the length of filament 2. Figure 13*a* and 13*b* show the [O III] and Hα emission, respectively. Figure 13*c* shows the [O III] image of filament 2 overdrawn with the contours of that image. The contours are logarithmic, with a factor of 2 difference in surface brightness between adjacent contours; the lowest level drawn is at an [O III] surface brightness of 1.68×10^{-6} ergs cm^{-2} s^{-1} sr^{-1}. Figure 13*d* shows the [O III] contours overdrawn on the Hα image.

As is apparent from the images, the characteristics of filament 2 change in a systematic way along its length, undergoing a transition from being Balmer-dominated at its southeast end to being weak or absent in Hα emission but strong in [O III] at its northwest end. There is a well-defined transition region visible in the images across which the Hα emission fades out as the strength of [O III] emission increases. The visible and UV spectrophotometry confirms this trend. This filament is analogous to the radiative filament studied by Raymond et al. (1988) in that the smooth structure of the filament and the gradual change in emission characteristics along its length indicate that conditions along the filament vary in a continuous fashion. Large or abrupt difference in preshock density along the filament would be apparent in the morphology of the structure.

We interpret the change along the length of Filament 2 as catching a portion of the blast wave as it is undergoing the transition from being a nonradiative shock to becoming radiative. Briefly, we find that at the southeast end the filament is nonradiative, and essentially indistinguishable from the other Balmer-dominated filaments in the region. At the northwest end, the shock velocity is somewhat lower and the column depth through the shock is enough higher that formation of the [O III] portion of the cooling region is well under way. Enough UV photons have been produced in the cooling region at the northwest end to fully preionize H atoms coming into the shock, which accounts for the drop in Hα emission as [O III] strengthens. The absence of a radiative component to Hα at the northwest end of the filament indicates that not enough cooling has occurred behind the shock for significant H recombination to take place. In the following sections we develop this picture of filament 2 more thoroughly.

4.4.1. *Variation in v_s, $N_{\rm H}$, and $X_{\rm H0}$ along Filament 2*

We begin by interpreting the *IUE* spectra and their associated [O III] and Hα fluxes using models which have a well-defined and nonvarying shock velocity, but with truncated cooling and recombination regions. In this approach, first employed by Raymond et al. (1988), the shock velocity is set by the strength of the highest ionization potential species (in this case N V and He II), while the column depth swept up by the shock is determined by the strength of lines (here, O IV], N IV], C III], and [O III]) which are formed in the cooler portions of the flow. In the earlier work, Raymond et al. were able to assume that the portion of the cooling region responsible for the hottest observed lines was complete, leading to an unambiguous determination of shock velocity. For these nonradiative shocks, however, this assumption is not valid, leading to some ambiguity in sorting out the effects of shock velocity and column depth.

In the present case the comparison is done using spectra and models which have been normalized to C IV $\lambda 1550 = 100$. In some respects this choice is not ideal. Initially, C IV is subject to attenuation by resonant scattering within the edge-on sheet of gas we observe. However, Long et al. (1992) show that this attenuation is only a few percent in filament 1. Also, as discussed above, the gas-phase carbon abundance may vary behind the shock because of progressive destruction of grains. On the other hand, there are respects in which C IV is uniquely suited as a comparison line. C IV is a strong line behind shocks with velocities throughout the range applicable to our data and is observed in all the spectra with good signal-to-noise ratio. In addition, the ionization potentials of C III (47.9 eV) and C IV (64.5 eV) place C IV intermediate between species such as O III (IP = 54.9 eV) and N V (N IV IP = 77.5 eV; N V IP = 97.9 eV), making C IV an ideal yardstick for measuring the relative strength of lines formed in both the hotter and cooler portions of the flow.

SWP 40306, which is at the southeast end of filament 2, is characterized by very strong N V and He II, with no additional lines other than C IV detected in the UV spectrum. The collisionally excited Hα emission is strong here as well, while [O III] is weak. The strength of the N V line requires $v_s > 170$ km s^{-1}, with some ambiguity as to how high the velocity might

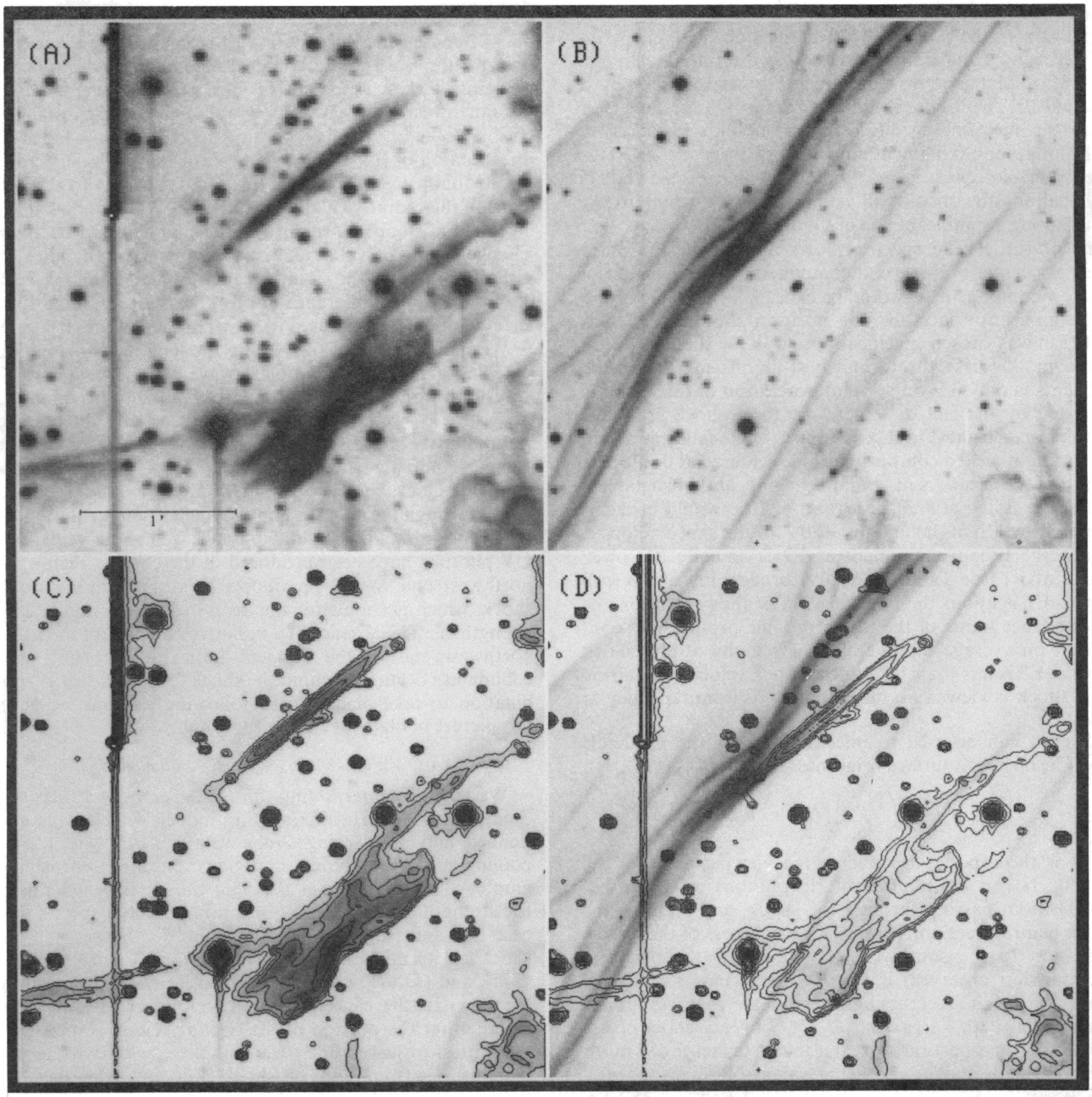

FIG. 13.—Blowups of the [O III] and Hα emission at filament 2. (*a*) A logarithmic display of the [O III] image. (*b*) A logarithmic display of the Hα image. (*c*) Surface brightness contours of the [O III] emission drawn on the [O III] image. The contours are logarithmic, with a factor of 2 difference in surface brightness between adjacent contours; the lowest level drawn is at an [O III] surface brightness of 1.68×10^{-6} ergs cm^{-2} s^{-1} sr^{-1}. (*d*) The [O III] contours overdrawn on the Hα image.

actually be. Using a model with $v_s = 180$ km s^{-1} and 30% neutral preshock H, the nondetection of lines "cooler" than C IV in the *IUE* spectrum and the weak [O III] requires $N_H < 4 \times 10^{17}$ cm^{-2}. The strength of the He II 1640 Å line, which is formed immediately behind the shock, would favor $N_H < 10^{17}$ cm^{-2}. The strong collisionally excited Hα at this location requires a substantial preshock neutral fraction.

SWP 21723 is positioned to the north-northwest of SWP 40306, following the Hα bright portion of filament 2 as shown in Figure 4. This spectrum is very similar to SWP 40306 and is probably indistinguishable within the estimated uncertainty of the line strengths. Using the same 180 km s^{-1} model, the strength of He II λ1640 relative to C IV still suggests $N_H < 10^{17}$ cm^{-2}, while the detection of [O II] λ3727 in the MMT spectrum (Table 4) favors $N_H > 4 \times 10^{17}$ cm^{-2} (although we will discuss below factors complicating interpretation of very weak lines of [O II] as well as [N II] and [S II] reported by FI). The weaker Hα at the position of SWP 21723 could also suggest a larger column depth (thereby increasing the strength of C IV relative to Hα), or perhaps a lower preshock neutral fraction. These spectra (SWP 40306 and SWP 21723) are similar to that reported by RBFG for filament 1 and represent a fairly "pure" nonradiative shock spectrum.

SWP 32368 is located just to the northwest of SWP 40306, following instead the western branch of filament 2 which becomes very bright in [O III]. The aperture was positioned just at the point along the filament where [O III] begins to become prominent. The *IUE* spectrum is also qualitatively different at this location, showing lines of O IV], N IV], and C III], in addition to an increase in the strength of [O III] by a factor of 4–14 with respect to the previous positions. While the strength of N V and He II at this location still requires $v_s \gtrsim 160$ km s^{-1} (assuming at 30% preshock neutral fraction), it becomes more difficult to cleanly separate the effects of shock velocity and column depth in this case. The spectrum could probably be equally well matched by a 160 km s^{-1} shock with $N_H \sim 4 \times 10^{17}$ cm^{-2} or a 170 km s^{-1} shock with $N_H \sim 7 \times 10^{17}$ cm^{-2}. Regardless of the value selected for v_s, however, it is clear at this location that temperatures in the cooling region drop to well below 10^5 K, and that observationally the shock is beginning to take on the character of a radiative shock (even if a drastically incomplete one). Hα is a factor of 3 weaker with respect to C IV at this location that at the location of SWP 40306, but is comparable to the location of SWP 21723.

SWP 37832 is the next position up the [O III] bright branch of filament 2. This position shows significantly weaker N V and He II than any of the positions to the southeast, as well as stronger O IV] and N IV]. The strength of N V could be accounted for by a shock as slow as 150–160 km s^{-1}. The strength of [O III] is up by a factor of 2 from the previous position. Overall, using the 160 km s^{-1} model (30% neutral), we need $N_H \sim 5 \times 10^{17}$ cm^{-2} to account for the strength of the cooler species. However, Hα is down by another factor of 2, which at this point begins to require a significantly lower preshock neutral fraction. This would somewhat reduce the required shock velocity.

SWP 37836 is located to the west of SWP 37832, and includes a slight extension to filament 2 which is visible in [O III] but not Hα. The strength of N V is comparable to SWP 37832, suggesting a similar shock velocity. Both O IV] and N IV] are up by a factor of almost 2 with respect to SWP 37832, C III] is strong, and [O III] is comparable to SWP 37832. The strength of Hα has fallen by an additional factor of 2. This spectrum generally fits the trend of decreasing inferred shock velocity, increasing column depth, and decreasing preshock neutral fraction along the filament.

4.4.2. *Shock Deceleration and Interpretation of Spectrophotometry*

In the preceding section we assumed that the shock velocity has remained constant since the first parcel of gas was shocked. This is probably not a good assumption. For example, in the case of SWP 37832, it would take a 150 km s^{-1} shock approximately 10^3 yr to accumulate a column depth of 5×10^{17} cm^{-2}. Thus, the gas responsible for most of the emission from lower ionization potential species was shocked 10^3 yr ago, while the gas responsible for N V and He II emission was shocked within the last 100 yr or so.

Rapid shock deceleration (which we argue below must have occurred in this region over the last 10^3 yr) significantly complicates interpretation of shock spectra because, while the lines formed a short distance behind the shock are telling us about the recent shock velocity, the overall emission spectrum represents and ensemble of shock velocities and evolutionary histories. For example, it takes approximately $260/n_0$ yr for a parcel of gas shocked by a 180 km s^{-1} shock to cool to the same temperature as that found immediately behind a 140 km s^{-1} shock. Assuming a preshock density of 1.2 cm^{-3} (§ 4.7.4), this takes 220 yr. If the shock itself has decelerated from 180 km s^{-1} to 140 km s^{-1} during this same period, then the postshock flow would consist of a column of about 1.2×10^{17} cm^{-2} of approximately *isolated* gas. This gas would be at the temperature ($\sim 2.8 \times 10^5$ K) characteristic of the immediate postshock conditions behind a 140 km s^{-1} shock. (The ionization state within the column could be more complex because of nonequilibrium ionization within the rapidly evolving flow.) A spectrum of the shock at this point might require that the shock velocity be little more than 140 km s^{-1} and show line ratios that require little accumulated column of gas behind the shock. The high surface brightness of the shock, however, could lead to a significant overestimate of preshock density.

In § 4.7.4 we will conclude that on average the shock has decelerated from $v_s \approx 400$ km s^{-1} to $v_s \approx 180$ km s^{-1} in the last 1000 yr. This is an average deceleration rate of ~ 0.22 km s^{-1} yr^{-1}. At this rate of deceleration it would take 180 yr for a 180 km s^{-1} shock to slow to 140 km s^{-1}. This is actually somewhat shorter than the 220 yr cooling time calculated above, suggesting that the scenario in the preceding paragraph may be common within this region. In fact, the presence of $2–4 \times 10^6$ K gas a short distance behind a shock front currently capable of heating gas to only a few times 10^5 K shows that all shocks in the region must pass through a phase during which the postshock temperature structure is inverted, with previously shocked gas cooling more slowly than the rate at which the postshock temperature is decreasing due to shock deceleration.

By evaluating the column depth required for material shocked at a higher shock velocity to cool to the immediate postshock temperature at the velocities inferred above then truncating the portions of the 180 km s^{-1} model which are *hotter* than this temperature, we can apply this concept in a rough way to the interpretation of the spectra of filament 2. Assuming that in all cases the "initial" shock velocity was 180 km s^{-1}, the spectra can probably be fairly well matched by a steady progression along filament 2 from $v_{\rm current} = 180$ km s^{-1} and $N_H \sim 10^{17}$ cm^{-2} at the southeast end of the filament to

$v_{current} = 150$ km s^{-1} and $N_H \sim 8 \times 10^{17}$ cm^{-2} at the position of SWP 37836.

Long et al. (1992) tried a similar approach by constructing a composite "summed" model, extracting different portions of the postshock flow from different velocity shock models. The principal difficulty with the fit of the summed model to their data is that lines from the lower ionization species are too strong. However, this model did not represent a thorough search of the range of plausible parameters for this region. In particular, given the extreme sensitivity of the strengths of low ionization lines to column depth in this regime, the strength of these lines is almost certainly a very strong function of the deceleration rate. Overall, we find the evidence very compelling that the shock has decelerated on time scales comparable to the cooling time and suggest that this must be an important aspect of understanding the current observed properties of these shocks. More generally, because of the dynamical nature of SNRs, the possibility of significant shock deceleration over cooling time scales is likely to be a common and important complication in interpreting shock spectra.

4.4.3. N v *from Cooling Coronal Gas?*

The spectrum at SWP 40295, which is the position farthest northwest along filament 2, is peculiar. Ignoring the emission from N v, this spectrum fits into the trend along filament 2 quite well. Emission from [O III] and O IV are strong, emission from He II is weak, and emission from Hα is very weak and may well arise in the incipient recombination region. All of this is consistent with a continuation of the trend to lower shock velocity and greater column depth moving to the northwest along the filament. N v, however, is stronger than would be expected for the position by at least a factor of 1.5.

SWP 40295 is located in projection well behind the leading edge of the line of filaments of which filament 2 is a part, in a region in which the HRI image shows strong X-ray emission. A plausible explanation for the strong N v at this location is emission from gas along the line of sight which was shocked sometime ago (when the shock velocity was higher) and is now emitting in N v. Such intermediate-temperature material behind the shock front seems an inescapable consequence of the recent history of the shock as discussed in the preceding section and below. This emission could in principle contaminate all of our UV spectra, making the shock velocities based on the strength of N v upper limits.

This problem could also complicate interpretation of the HUT spectrum of filament 1 discussed by Long et al. (1992). The HUT slit is 9.″4 wide, which means that a substantial amount of emission from well behind the shock is included in the spectrum. That region is very bright in the HRI images, and it is expected that O VI emission should correlate well with soft X-ray emission. Existing work on the distribution of O VI in the Cygnus Loop (Blair et al. 1991a; Rasmussen & Martin 1992) shows that O VI emission correlates well with the X-ray emission over larger spatial scales than are discussed here. In addition to allowing for a lower "current" shock velocity, significantly contamination of the HUT spectrum by emission not arising immediately behind the shock front would help to reconcile the preshock density of 4–10 cm^{-3} inferred by Long et al. with the values of less than 3 cm^{-3} inferred in this paper and by RBFG.

4.4.4. *Effect of Radiation on Preshock Neutral Fraction*

Above we noted that the increasing importance of the cooling region in the sequence of spectra moving from southeast to northwest along filament 2 was accompained by a decrease in the preshock neutral fraction. The long-slit MMT spectrum confirms this trend. Examining the line strengths normalized to He II λ4686 (which should be less affected by differences in the radiation), Table 6 shows that the strength of Hα drops by a factor of 5 over the same portion of the slit (roughly 30″ long) along which [O III] increases by a factor of 10.

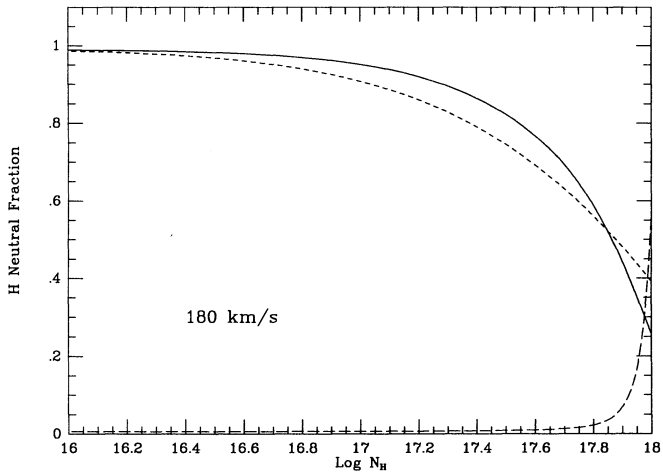

FIG. 14.—Calculation of ionization of the preshock medium by the radiative precursor of a 180 km s^{-1} shock. The solid line shows a preshock H neutral fraction as a function of the column depth swept up by the shock. The short dashed line shows the preshock He neutral fraction. The long-dashed line shows the accumulated [O III] emission in units of 10^{-5} ergs cm^{-2} s^{-1}.

A possible explanation for the inverse relationship between column depth and preshock neutral fraction is that UV radiation from the newly formed cooling region is able to photoionize the preshock medium. Shull & McKee (1979) considered the implications if the preshock medium were assumed to be in photoionization equilibrium with UV escaping from a fully radiative shock front. To explore this possibility in the current context of nonsteady flow shocks, we used the shock models described in § 3.2 to quantitatively evaluate the effect of radiation on the ionization of the preshock medium. Figure 14 shows the result of this calculation for a 180 km s^{-1} shock. The solid line shows the preshock H neutral fraction, including the effects of photoionization by the UV formed in the cooling region, plotted as a function of column depth swept up by the shock. The short dashed line shows the preshock He neutral fraction. The long-dashed line shows the accumulated [O III] emission from the shock in units of 10^{-5} ergs cm^{-2} s^{-1}. As can be seen, the preshock neutral fraction is falling rapidly at the column depth where [O III] emission is becoming strong. This is in good agreement with the observation for filament 2 that the collisionally excited Hα emission fades just as the [O III] emission brightens, and confirms the causal relationship between formation of a postshock cooling region and supression of collisionally excited Balmer-line emission from the shock.

4.5. *Knots of Bright* [O III]

The [O III] emission in the field is dominated by four or five regions, typically a couple of arcminutes in size, in which [O III]/Hβ can exceed 100. (A good example appears in the southwest corner of the field shown in Fig. 13.) This is characteristic of drastically incomplete cooling behind a radiative

shock (e.g., Raymond et al. 1980). These features appear to mark locations where the blast wave has encountered localized regions of higher density that are about a parsec in size. In all cases weak radiative Hα emission is seen only in the central trailing portions of a feature, because it is here that the shock has swept up the largest column of gas since hitting the cloud. (See Figs. 7 and 8 from Hester 1987.)

The difference between these regions and filaments 1 and 2 may be only a matter of degree. Given the fact that the blast wave as a whole through this region is close to becoming radiative, it may take only a slight density increase to given rise to [O III] bright regions such as these. In this case, the difference between the smooth morphology of filaments 1 and 2 and the more "tangled" appearance of the [O III] bright filament complexes could be due to the development of thermal instabilities behind the shock.

4.6. *Line Profiles of the Balmer-dominated Emission*

4.6.1. *The Narrow Broad Component: Rapid Equilibration or Shock Deceleration?*

The widths of the broad components of the Hα line profiles of the Balmer-dominated emission are generally significantly smaller than previously reported. In particular, the measured width of the broad component of the Hα line at filament 1 is 130 km s^{-1}, compared with 167 km s^{-1} as reported by RBFG. The much higher quality of our data and the fact that four different spectra all give widths in the range between 117 km s^{-1} and 134 km s^{-1} seem to make this a very firm result. The only position with a profile significantly broader than 130 km s^{-1} is the east end of the slit through filament 2 (E3). It is perhaps not coincidental that this is also the position with the weakest [O III] emission.

For a number of reasons, RBFG favored a model for filament 1 in which the ion and electron temperatures equilibrate slowly behind the shock by way of Coulomb interactions. However, if postshock equilibration is slow, then the observed width of 130 km s^{-1} for filament 1 would imply $v_s = 130$ km s^{-1}. This is in contrast to the strength of N V and He II emission at the location which requires that the postshock flow be more characteristic of that behind a 170 km s^{-1} shock.

One possible way to resolve the discrepancy between these results is to assume rapid postshock equilibration of T_i and T_e. In this case the shock velocity is 1.25 times the FWHM of the broad component, and the width of the line profile at filament 1 would imply a shock velocity of 163 km s^{-1}, which is marginally consistent with the results of the spectrophotometry. Similarly the ratio of the broad to narrow component at filament 1 (1.34) is in better agreement with the Smith et al. (1993a) calculation for a fully equilibrated 180 km s^{-1} shock than for a 135 km s^{-1} shock with Coulomb equilibration. It is tempting on the basis of these data to conclude that T_i and T_e are rapidly equilibrated behind the shock (Hester & Raymond 1988). A similar conclusion was suggested by Long et al. (1992).

The issue of the history of the shock front calls this conclusion into question, however. In § 4.4.2, we found that it is probably common for the ionization state of postshock gas to drop faster as a result of shock deceleration than cooling can reduce the ionization state of gas shocked at an earlier time. In this case, shock velocities based on the strength of UV emission from high ionization potential species are upper limits to the current shock velocity. Thus, the strength of N V emission which seems to require a shock velocity of 180 km s^{-1} really requires only that the shock velocity was in excess of 180 km s^{-1} sometime within the last few hundred years. Given the inferred rate of shock deceleration in the field studied, it seems plausible that a shock with a current velocity of 130 km s^{-1} would still show significant N V emission. Were this the case it could reconcile the Hα line width with Coulomb equilibration. In the end, all that we can safely conclude is that the question of Coulomb versus rapid equilibration behind Balmer-dominated shocks in the Cygnus Loop has yet to be resolved.

4.6.2. *The Broad Narrow Component: Evidence for a Shock Precursor*

Treffers (1981) and RBFG reported that the narrow components of the Hα line profiles in the positions which they measured appeared to be somewhat broader than their instrumental resolution. Our results confirm this observation. All of the positions measured had narrow component widths of order 33 km s^{-1}, including the spectrum obtained with the 100 μm slit, in which the narrow component was well resolved. If thermal, a FWHM of 33 km s^{-1} corresponds to a temperature of 25,000 K for the gas entering the shock front.

Based on the kinetic model described in § 3.1, we found that radiative transfer effects cannot account for the observed 33 km s^{-1} width of the Hα line profile. Similar widths have been observed in four Balmer line remnants in the LMC having much higher shock velocities (Smith et al. 1993b). Thus we conclude that this width of the narrow component of the Hα line is attributed to a precursor, the basic requirements are that the neutrals be given a velocity dispersion (thermal or nonthermal, possibly by way of charge transfer with ions) of about 33 km s^{-1} without all being ionized. There are several possibilities, which are also discussed in Smith, et al. (1993b).

1. The upstream gas is ionized and heated by photons from the postshock gas. If the ionizing photons are fairly hard, such as the very strong He II λ304 line, then a substantial amount of heat is deposited in the electrons. The main difficulty is that the thickness of the photoionization precursor, which is determined by the photoionization cross section of H, is large enough that there is likely to be time for collisional processes to ionize most of the hydrogen. It may be possible to overcome this difficulty by limiting the amount of time that the preshock medium has been exposed to the radiative precursor, as would be consistent with rapid dynamical evolution of the region. However, four Balmer-dominated remnants in the LMC all show similar narrow component widths (Smith et al. 1993b), so it is troublesome to appeal to a special time in the shock evolution. If gas currently entering the shock has been heated significantly by the radiative precursor, but has not yet been fully ionized, then the heating of preshock neutrals would be analogous to the heating of neutrals in the postshock gas. Electrons would have to share their energy with protons, which would then charge transfer with neutrals. For a radiative precursor to effectively heat the preshock neutrals, the process would have to be more efficient than collisional ionization.

2. A thermal conduction precursor can occur if the shock velocity is lower than the electron thermal velocity (Zel'dovich & Raizer (1968). As with the radiative precursor this is an inefficient way to heat neutrals without ionizing them, but again if the precursor has only recently been "turned on," it is possible that the preshock gas has not been ionized *yet*. However, this precursor is likely to be so thin that the electrons cannot heat the neutrals to the observed temperature (Smith et al. 1993b).

3. An MHD precursor, along the lines of those suggested by Draine (1980), will move ahead of the shock if the Alfvén velocity in the preshock ionized gas is larger than the shock velocity. The existence of such a precursor has been suggested by Graham et al. (1991) to account for H_2 emission from the vicinity of fast shocks to the south of this field. In the present case an MHD precursor implies either an uncomfortably high magnetic field or an uncomfortably low ionization fraction. Assuming a preshock density of 1 cm^{-3}, $v_A = 200$ km s^{-1} would require $B/(X)^{1/2} = 100$, where B is in μG and X is the preshock ionization fraction. For a preshock field of 1 μG, this would require a preshock ionization fraction of 10^{-4}, which is almost certainly inconsistent with the radiation environment as well as the preshock ionization fraction inferred from spectrophotometry. Similarly, a more reasonable preshock ionization fraction of 0.5 would require $B = 70$ μG in front of the shock.

4. A precursor in which cosmic rays are trapped between the shock front and a region of strong Alfvén waves is a vital component of Fermi models of particle acceleration in shocks (Blandford & Eichler 1987). Boulares & Cox (1988) have developed specific models for the Cygnus Loop, and these provide substantial preshock heating. At present the models are quite ambiguous because the precursor thickness scales with the diffusion coefficient, which is unknown.

The constraint that the precursor be thin enough that H remains partly neutral at 25,000 K requires a thickness satisfying $d < v_s/n_e q_i$, where q_i is the collisional ionization rate for hydrogen. The thickness is also given by $d \simeq k/v_s$, where κ is the cosmic-ray diffusion coefficient (Blandford & Eichler 1987), so that κ must be less than about 10^{25} cm^2 s^{-1}/n_0. A lower limit to the diffusion coefficient can be obtained by assuming that the observed line width corresponds entirely to Alfvén turbulence, assuming equipartition between magnetic and kinetic energy in the Alfvén waves, and employing equation (5.1) of Blandford & Eichler (1987). The result is $\kappa > 10^{23}$ cm^2 s^{-1}. The Boulares & Cox (1988) model for the Hα filaments assumes that cosmic rays dominate the shock energetics. It predicts that the temperature rises smoothly through the precursor to over half the postshock value. This would remove the distinction between broad and narrow components. A shock which converts a modest fraction of its energy of cosmic rays might predict the observed modest precursor temperature.

5. The charge transfer process which creates the broad component of Hα does so by creating a population of neutrals with the postshock ion kinetic distribution. As modeled in § 3.1, a few percent of these overtake the shock, move ahead of it, and deposit their energy when they charge transfer with upstream ions. The advantages of a fast neutral precursor are that such a precursor must accompany a Balmer-dominated shock, and unlike most potential precursors, a fast neutral precursor will efficiently heat preshock neutrals via charge exchange reactions. However, while the amount of energy carried by the fast neutral precursor is not too different from that required by the line profiles ($\sim[33/135]^2 = 6\%$ of the thermal energy of the postshock neutrals), much of the energy flux is advected back through the shock before it can heat the narrow component neutrals. Smith et al. (1993b) argue that the heating in such a precursor is sensitive to preshock neutral fraction, shock velocity, and electron-ion equilibration, so that such precursors are unlikely to account for the similar narrow component widths observed in the Cygnus Loop and the four LMC Balmer line remnants. It remains possible, however, that a feedback due to reduced neutral fraction if the temperature becomes too large can reconcile this picture with the observations.

The weak emission from [N II] and [S II] reported by FI for filament 1 and the strength of [O II] in our spectra poses a problem for nonradiative shock theory. The column depth accumulated to date by the shock at Filament 1 is far short of that required to produce any significant emission from these low-ionization species. Heating of the preshock medium by a precursor may offer a solution to this problem. If [N II] emission is assumed to be 1% of Hα at filament 1, then the face-on Hα surface brightness inferred above requires that the precursor produce 6500 photons per second per cm^{-2} of shock surface area. Assuming an N abundance of 1×10^{-4}, a 70% preshock N^+ fraction (matching that of H), $T = 20{,}000$ K, and an N^+ ^3P, ^1D collision strength from Osterbrock (1989), the zone of [N II] emission in the precursor need only be $\sim 10^{16}$ cm thick to account for the observed emission. This is somewhat larger than the expected thickness of a precursor heating the preshock medium via charge exchange reactions with the preshock medium set by the charge transfer mean free path ($\sim 10^{15}/n_0$ cm), but within the broad range allowed for a cosmic-ray precursor.

4.7. *The History of the Shock*

4.7.1. *Shock Reflection from a Cavity Wall*

Above we have invoked the possibility of recent deceleration of the shock front a number of times. Evidence to support this view includes the discrepancy among the low shock velocity inferred from Hα line profiles, the higher shock velocity inferred from UV spectra, and the still higher shock velocity inferred from X-ray temperatures. The very small separation between the Balmer-dominated shocks and the edge of the bright X-ray emission requires that the deceleration was abrupt. Hester & Cox (1986) also argued that deceleration of the shock in this region is required to convert the momentum of the postshock gas into pressure to account for the brightness of the X-ray emission, and well as the very sharp limb brightening which requires the existence of a fairly thin zone of bright X-ray emitting material behind the shock. In addition, the remarkably smooth morphology of the emission in the region, despite evidence that shock velocities vary significantly within the field, requires that deceleration was recent. Filaments 1 and 2 appear to lag their surroundings by less than 10″. Assuming a velocity difference of order 40 km s^{-1}, we conclude that filaments 1 and 2 slowed with respect to their surroundings within the last 800 yr.

Together, these data are easiest to understand if the current locus of the shock is determined principally by the location of the wall of a preexisting cavity which was hit by the SN blast wave only recently. The view that the Cygnus Loop is the result of a cavity explosion is not new (e.g., McCray & Snow 1979; Charles, Kahn, & McKee 1985; Braun & Strom 1986). To explore this possibility, we consider the case of the shock wave encountering a step in preshock density, leading to transmitted and reflected shocks.

4.7.2. *Calculation of the Structure*

Figure 15 shows a sketch of a shock hitting a density jump before and after the encounter. Subscript 0 refers to preshock conditions and shock velocity prior to the density jump. Subscript 2 refers to postshock conditions at this time. Subscript 1 refers to preshock conditions and the shock after the shock has

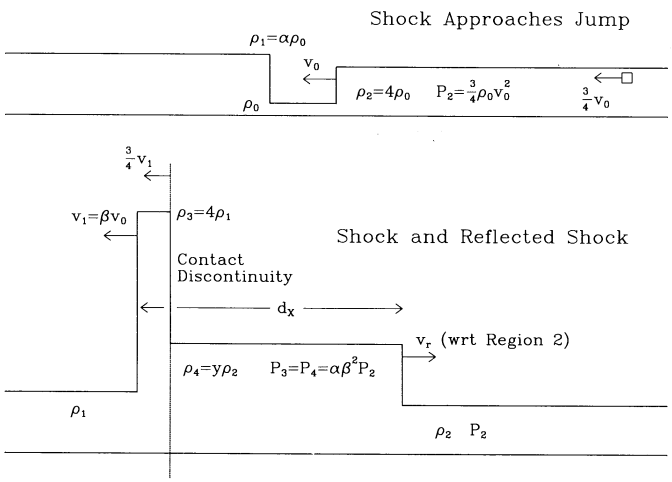

FIG. 15.—A sketch showing the situation before and after a shock reaches the location of a jump in preshock density, showing the convention for subscripts and symbols used in the text.

hit the density jump. (During the current epoch, $v_1 = v_s$, where v_s is the observed shock velocity discussed throughout the paper.) There is a contact discontinuity between region 3, which consists of postshock material originating in region 1, and region 4, which consists of material behind the reflected shock driven back into region 2.

Using these conventions, we solved the standard equations of conservation of mass, energy, and momentum across the primary and reflected shocks, and required pressure balance across the contact discontinuity. We assumed that the density jump is sharp, that the postshock region is uniform, and that the preshock pressure can be ignored. We also ignored ionization and magnetic fields in the energy and momentum equations. Using the definitions $\alpha = \rho_1/\rho_0$, $\beta = v_1/v_0$, $\eta = v_s/v_0$, and $y = \rho_4/\rho_2$, the solution of these equations, together with standard strong shock relations relating quantities subscripted 0 and 2, gives

$$\alpha(\alpha - 4)\beta^3 + 8\alpha\beta^2 - (6\alpha + 1)\beta + 2 = 0 ,$$

which can be solved for $\beta = \beta(\alpha)$. Other quantities such as the pressure, density, and temperature ratios among the various zones and the relative velocity of the reflected shock can be calculated in terms of α and β, viz.,

$$\eta = \frac{(\alpha\beta^2 - 1)}{4(1 - \beta)} , \quad \frac{1}{y} = 1 - \frac{3}{4\eta(1 - \beta)} ,$$

$$P_2 = \frac{3}{4}\rho_0 v_0^2 , \quad P_3 = \alpha\beta^2 P_2 , \quad \frac{T_4}{T_2} = \frac{\alpha\beta^2}{y} .$$

Assuming that the ionization energy is not important behind the original fast shock gives

$$T_2 = 1.44 \times 10^5 (v_0/100)^2 \text{ K} ,$$

where v_0 is expressed in units of km s^{-1}. Figure 16 shows various quantities plotted as a function of $\log_{10}(n_1/n_0)$.

4.7.3. *Applying Constraints*

Four quantities are required in order to specify the system: (1) some measure of the shock velocity; (2) some measure of the density; (3) some measure of the time since the shock hit the density jump; and (4) the magnitude of the density jump, α. Most of the quantities that can be measured or estimated from line widths, spectra, surface brightnesses, or physical scales constrain the system in some way. A consistent fit to all of the

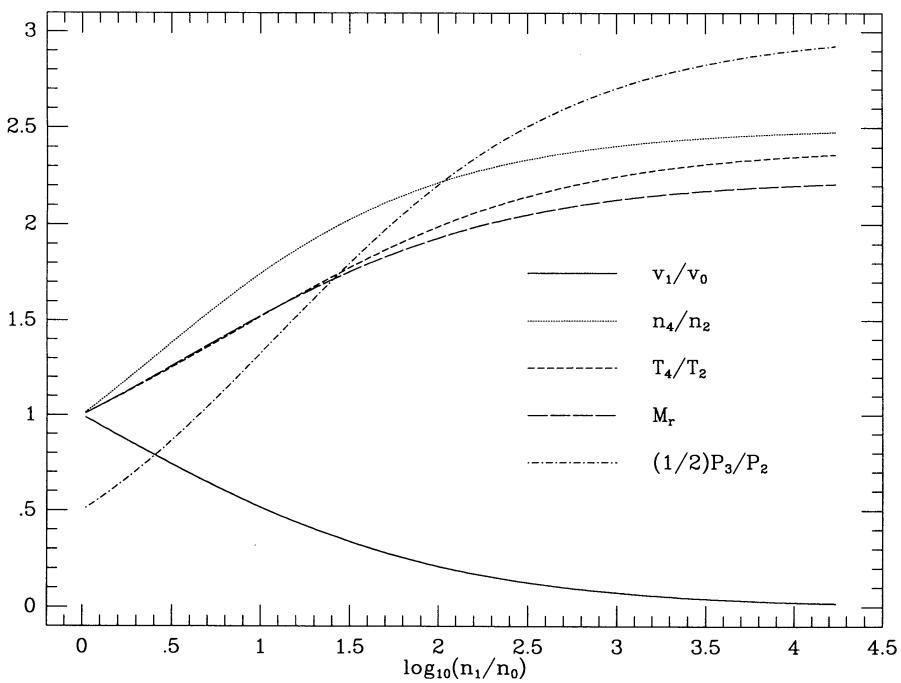

FIG. 16.—Characteristics of the main shock and the reverse shock following the interaction of the SN blast wave with a density step as a function of the density contrast across the step. The ratio of the velocity of the main shock after the interaction to that of the original shock is given as v_1/v_0. M_r is the Mach number of the reverse shock. The other quantities are the ratio of densities, temperatures, and pressures across the reverse shock. See Fig. 15 for definitions of the subscripted regions. Note that $(1/2)P_3/P_2$ is plotted. The pressure ratio approaches 6 for very large density contrast.

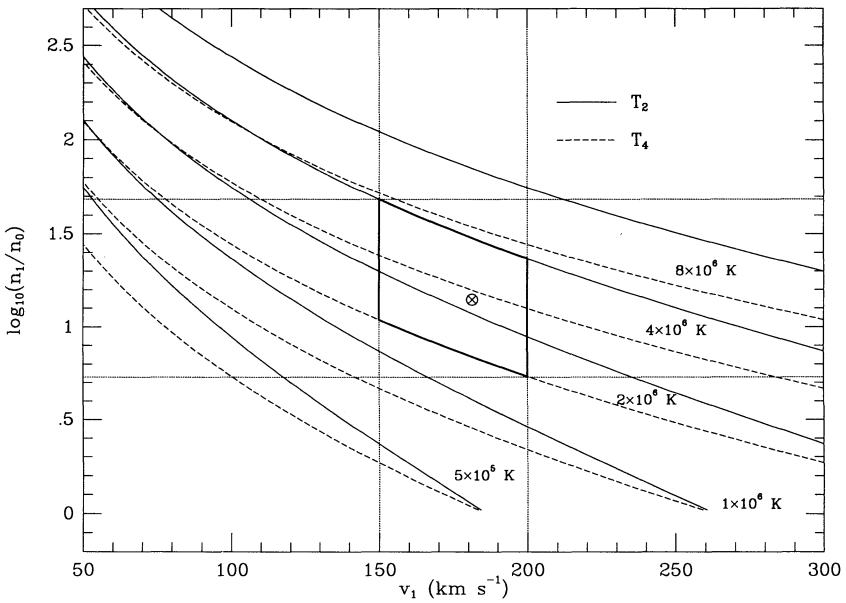

FIG. 17.—A plot showing contours of constant temperature in the plane defined by the density contrast across the jump in preshock density and the velocity of the primary shock wave after hitting the density jump. The solid lines show contours of constant temperature T_2 in the postshock gas which has not yet been hit by the reverse shock. The dashed lines show contours of constant temperature T_4 in the region behind the reverse shock. Curves are shown for temperatures between 5×10^5 K and 8×10^6 K in steps spaced by factors of 2. The behavior is such that increasing the density contrast decreases the shock velocity required to reach a given temperature in the zone between the shocks. The dotted vertical lines show the constraint 150 km s^{-1} < v_1 < 200 km s^{-1} obtained from UV and optical spectrophotometry and the Hα line profiles. The temperature constraint $T_2 < 4 + 10^6$ K and $T_4 > 2 \times 10^6$ K comes from the X-ray temperature inferred from *Einstein* observations. The heavy lines outline the region in the plane consistent with these constraints. The dotted horizontal lines show the range of density contrast consistent with these constraints. The crossed circle indicates what we take as a representative model with $v_1 = 180$ km s^{-1} and $n_1/n_0 = 14$.

observational data is then a good test of the validity of the model.

Figure 17 shows contours of constant T in the X-ray emitting regions 2 and 4 in a plot of $\log_{10}(n_1/n_2)$ versus v_1. The X-ray temperature in the Cygnus Loop is typically in the range 2–4 × 10^6 K (Ku et al. 1984). It is unclear which of the two regions is being probed, but it seems likely that T_4 (the temperature in the hot reshocked region) exceeds 2×10^6 K, while $T_2 < 4 \times 10^6$ K.

The average shock velocity in the region ($v_1 = v_s$) is constrained by spectrophotometry and by the [O III]/Hα ratio from the imagery. From Table 7 the ratio $I_{[O\,III]}/I_{N\,V} = 0.017$ at the position of RBG/FG. The [O III] and Hα images indicate that the average value of $I_{[O\,III]}$/Hα for the Balmer-dominated emission in the field is about half that of filament 1, which (assuming that the increase in [O III] is due to the onset of radiative cooling) suggests that the average value of $I_{[O\,III]}/I_{N\,V}$ may also be lower by a factor of 2. The ratio of $I_{[O\,III]}/I_{N\,V}$ for the Balmer-dominated portion of filament 2 (Table 5) is 0.011, intermediate between these values. Using models with 30% preshock neutral H, the ratio implies that $v_1 > 150$ km s^{-1}. Overall, the data seen to require 150 km s^{-1} < v_1 < 200 km s^{-1}, which is also what we would surmise from assuming that the shocks studied in detail in § 4.4 are generally a bit lower velocity than average for the region.

When these constraints are imposed on Figure 17 they define a region which requires $5.4 < n_1/n_0 < 50$. Representative values are $v_1 = 180$ km s^{-1} and $n_1/n_0 = 14$, corresponding to $T_2 \gtrsim 2 \times 10^6$ K and $T_4 \lesssim 4 \times 10^6$ K.

The column density swept up since the jump, $N_H = n_1 v_1 t$, is constrained directly by the UV and optical spectroscopy. If the column depth is too low there is no radiative contribution to [O III], and $I_{[O\,III]}/I_{N\,V}$ is too small. If the column depth is too high, the radiative contribution to [O III] makes $I_{[O\,III]}/I_{N\,V}$ too large. This is a tight constraint. For $v_1 = 180$ km s^{-1}, the factor of 2 range in the line ratio given above requires that $N_H = 5$–6×10^{17} cm^{-2}. For a 160 km s^{-1} shock, $0.017 > I_{N\,V}/I_{[O\,III]} > 0.009$ requires $N_H = 2.2$—2.8×10^{17} cm^{-2}.

The distance d_X from the main shock to the back of the X-ray bright region (which is assumed to trace the reflected shock) is ambiguous due to low signal-to-noise ratio, confusion with limb brightening, and confusion among the two major tangencies across the center of the field. A conservative constraint seems to be $30'' < d_X < 2'$. Errors in d_X effect computed values for n_1 and for t. Since v_s is set by v_1 and α, $t \propto d_X$. Since N_H is constrained, $n_1 \propto t^{-1} \propto d_X^{-1}$.

4.7.4. *A Model*

Having established the model parameters $v_1 = 180$ km s^{-1}, $N_H = 6 \times 10^{17}$ cm^{-2}, and $d_X = 1' = 7 \times 10^{17}$ by application of the observational constraints in the previous section, Figure 18 shows a number of additional quantities plotted against $\log_{10}(n_1/n_0)$. We have assumed a distance of 770 pc to the Cygnus Loop (Minkowski 1958). B_X is the enhancement of the X-ray brightness across the reflected shock, assuming that the emissivity scales as n^2 and is not a strong function of temperature. The curves for preshock density, B_X, and the X-ray temperature converge near their observed values for a value of $\alpha = n_1/n_0 = 14$. At this point, $B_X \sim 3$, $n_1 \sim 1.2$ cm^{-3}, $n_0 \sim 0.09$ cm^{-3}, $v_0 \sim 400$ km s^{-1}, $P_4/P_2 \sim 3$, and $t \sim 1000$ yr. The reflected shock has $v_r \sim 400$ km s^{-1}, and has a Mach number of 1.6.

These values agree with additional observations, as well. The standard values used to describe the X-ray emission from the

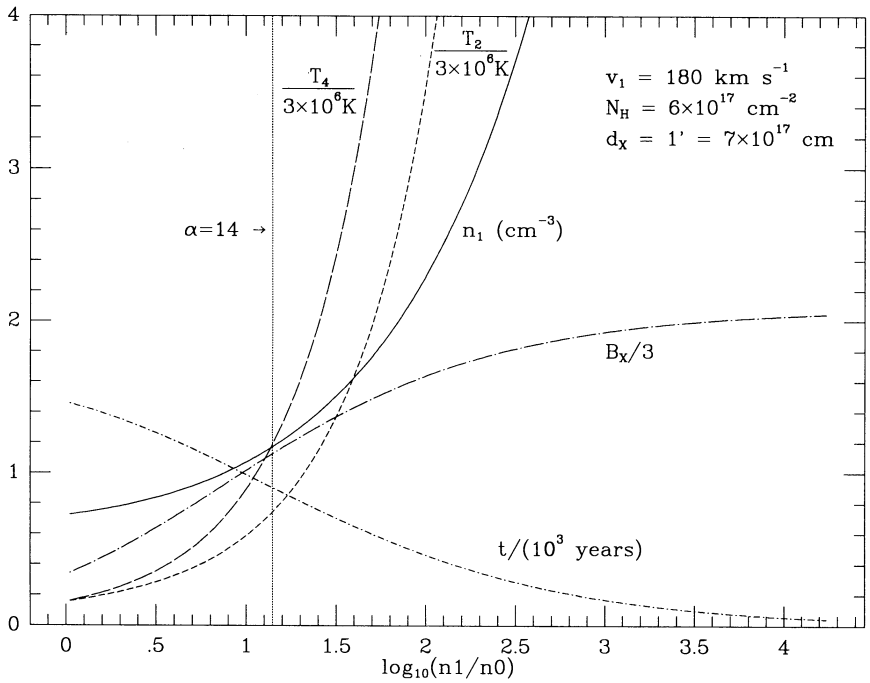

FIG. 18.—Plots of X-ray temperatures (T_2 and T_4), current preshock density (n_1), increase in X-ray emissivity across the reverse shock (B_X), and time since the shock wave hit the density jump (t) as a function of the original density contrast across the jump. All quantities except t are directly constrained by observations and are normalized by values consistent with observational data. The model used $v_1 = 180$ km s^{-1}, $N_H = 6 \times 10^{17}$ cm^{-2}, and $d_X = 7 \times 10^{17}$ cm. The vertical dotted line shows the solution for $n_1/n_0 = 14$, which matches all of the observational data to well within observational uncertainties.

Cygnus Loop are $n_0 = 0.16$ cm^{-3} and $v_0 = 300$–400 km s^{-1} (Ku et al. 1984). Since the X-ray emission is dominated by the region between the main and reverse shocks, the preshock density which *would* be inferred from this region, *ignoring the presence of the reverse shock*, is $n_0(P_A/P_3)^{1/2} = 0.15$ cm^{-3}, in good agreement with the canonical value. The very rapid deceleration of the shock in the model explains the otherwise puzzling fact that the X-rays extend up to the Balmer-dominated filaments. For the model parameters presented above, the X-ray emission should begin at the contact discontinuity which is located $\frac{1}{4}v_s t$, or about 10″, behind the shock. The value of n_1 is also in good agreement with $n_1 = 2$ cm^{-3} inferred from the *IUE* spectra (RBFG) and the value of $n_1 < 3$ cm^{-3} inferred above from the Hα surface brightness and limits on the viewing angle.

The assumptions made here are certainly simplifications over the real situation. It is more likely that the shock is running up a steep density gradient at the edge of the cavity (e.g., Shull et al. 1985), and that the shock velocity is continuously slowing. This would have the effect of blurring the boundary defined by the contact discontinuity in the model, as well as justifying the arguments above which assume that deceleration has continued until the present epoch. The pressure drop due to radiative losses must also begin to be important, given our conclusion that the shock is entering the radiative phase. This will lead to further shock deceleration, as well as a pressure gradient across region 3. Radiative losses will also result in compression of the postshock gas, which will reduce the separation between the shock and the edge of the X-ray emission.

Despite these complications, however, the case of a simple reflected shock captures the essential physics of converting postshock momentum into pressure as the shock slows in response to increasing preshock density, and the calculation presented here shows that this effect is very successful at explaining a suite of apparently discrepant values for the shock velocity and preshock density in this region. Overall, we conclude that the body of existing observational data on the portion of the limb of the Cygnus loop can be well fitted by a model in which the SN shock expanded within a preexisting cavity with $n \approx 0.1$ cm^{-3} until about 1000 yr ago, when the shock hit a wall with $n \approx 1$ cm^{-3}.

This model of the Balmer-dominated portions of the northeast limb of the Cygnus Loop and its relationship to the observations is presented in Figure 19, together with various aspects of our interpretation discussed in earlier sections.

4.7.5. *The Fate of the Region*

This model is good only until the reflected shock has had time to cross the shell of swept-up material behind the blast wave, which has a width of about $R_{SNR}/12 = 5 \times 10^{18}$ cm. In the model the reflected shock has traveled $v_r t = 1.26 \times 10^{18}$ cm, or about $\frac{1}{4}$ of the way back through the swept-up shell. This indicates that the X-rays in this region will continue to brighten for another few thousand years, after which they will decay on a similar time scale as the overpressure between the shocks dissipates at the sound speed of the postshock gas. This evolution may be characteristic of the evolution of SNRs from Type II supernovae. Since the massive progenitors of these events are generally expected to form bubbles in the surrounding medium (e.g., Shull et al. 1985), the X-ray (as well as radio and optical) emission from Type II remnants should in general get very bright for a short time when the expanding blast value

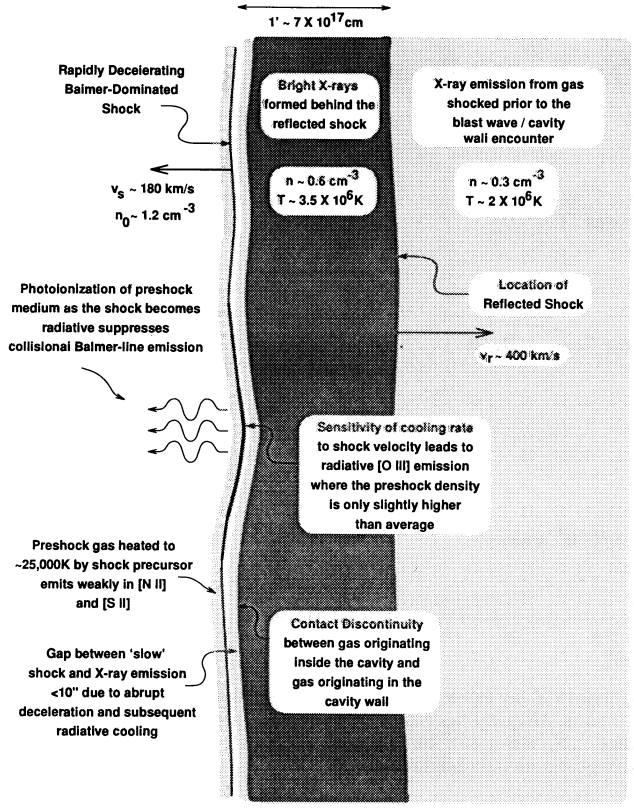

FIG. 19.—A summary of our model of the Balmer-dominated portion of the northeast limb of the Cygnus Loop. The sketch shows the region as it exists today, ~1000 yr after the shock hit the wall of a preexisting cavity. The shock velocity and preshock density today are typically ~180 km s^{-1} and 1.2 cm^{-3}, respectively. Prior to hitting the cavity wall the shock velocity was ~400 km s^{-1}, with a preshock density of ~0.09 cm^{-3}.

hits the wall of the cavity. Remnant properties inferred from models that neglect shock reflection will be inaccurate. For example, explosion energies inferred from Sedov fits to remnants caught during their bright phase will be larger for explosions that occurred with larger cavities. This would also affect estimates of supernova rates inferred from remnant populations.

The swept-up column required for a shock to become radiative is roughly proportional to v_s^4. So, assuming the ρv_s^2 is constant, the time required for cooling is proportional to v_s^5, or $\rho^{-5/2}$. In the present case, we found above that a shock with $n_0 = 1.2$ cm^{-2} cm^{-3} and $v_s = 180$ km s^{-1} starts to become radiative in approximately 1200 yr. For a shock with $v_s = 135$ km s^{-1} (requiring a preshock density of only about 2.1 cm^{-3}) the shock will start to become radiative in under 300 yr.

Because of the sensitivity of cooling time to preshock density and shock velocity, the regions which show strong [O III] emission need differ from their surroundings by only slight amounts. This same conclusion can be reached from morphological arguments, because if the density of regions such as filaments 1 and 2 differed much from their surroundings they would not join in so smoothly with the overall network of Balmer-dominated filaments. Together, the time scales for cooling and the apparent continuity of the structure suggest that the shock front is everywhere only a few hundred years from becoming radiative. Thus, over the next ~1000 yr the Balmer-dominated northeast limb of the Cygnus Loop can be expected to undergo a transition to a region resembling the bright radiative northeast or west limbs.

4.8. *Emission between the Bright Radiative Limb and the Balmer-dominated Shocks*

The region extending about 5′ northeast from the edge of the bright radiative filaments in the southwest corner of the field is filled with emission which is morphologically very different from either the Balmer-dominated filaments further to the northeast or regions of strong radiative shocks (e.g., Fig. 1 and Hester, Parker, & Dufour 1984). In [O III] this region shows tangled filamentary emission and diffuse emission, with filaments oriented at all directions, including several filaments oriented radially with respect to the SNR. The morphology still suggests that the [O III] is distributed in a surface, but unlike the other region, here the surface is disturbed and apparently fragmented on relatively small ($\sim 10^{17}$ cm) scales. The Hα image also shows a chaotic tangle of filaments in this region, but with the addition of more clumpy emission than is apparent in [O III]. This includes a very sharp Hα filament that is approximately 1′ long and is oriented almost exactly radially. This emission appears to be situated along the surface of the shock connecting the bright radiative shocks with the Balmer-dominated region (see Fig. 12) and is located near the intersection of the SNR blast wave and the cloud responsible for the bright northeast rim of the Cygnus Loop.

The [O III]/Hα ratio varies tremendously from filament to filament within this region, with the overall [O III]/Hα ratio about a factor of 20 higher than typical for Balmer-dominated shocks. This indicates that the emission is primarily due to cooling behind the shock. The radiative nature of the emission from the region between the Balmer-dominated shocks and the bright northeast limb of the Cygnus Loop is confirmed by the echelle spectrum, which shows [N II] emission with the same general distribution as the Hα emission. The echelle spectrum also shows structures which are contiguous in position-velocity space, which is characteristic of emission from a well-ordered shock front (Hester 1987; Raymond et al. 1988). In particular, the smooth diffuse region of emission visible just to the west of the center of the slit in Figure 4 appears in the echelle spectrogram as a smooth structure displaced from 0 velocity by 33 km s^{-1}. This indicates that the emission here is from a single crossing of a shock that is being viewed somewhat face-on. The displacement of all of the observed emission to the red indicates that the emission throughout this region is on the back side of the remnant.

From the images, we determined that the Hα surface brightness in this region is 8.4×10^{-6} ergs cm^{-2} s^{-1} sr^{-1}, and the [O III]/Hβ ratio is ~1.2. Using the method of Cox & Raymond (1985), this ratio implies a shock velocity into a fully preionized medium of 60–70 km s^{-1}, or a shock velocity into a fully neutral medium of 95–100 km s^{-1}. Since we have no independent constraint on the preshock neutral fraction, we can say only that 60 km $s^{-1} \leq v_s \leq 100$ km s^{-1} at this location. Thus the observed velocity of 33 km s^{-1} indicates that we are viewing the shock at an angle of 57°–71° from face-on.

The technique described by Raymond et al. (1988) can be used to determine the total ram pressure at this location. Briefly, this argument holds that since $I_{obs} v_{obs}$ is independent of viewing angle, that

$$I_{obs} v_{obs} = I_0 v_s = (K n_0 v_s) v_s = \phi \rho v_s^2 ,$$

where I_0 is the face-on surface brightness of the shock, v_s is the

shock velocity, and K and ϕ are quantities that are determined from shock models. While in principle $\phi = \phi(n_0, v_s, B_0, \ldots)$, in practice ϕ varies very little with respect to these parameters for a number of lines. For example, using the set of models published by Raymond (1979) with 60 km s^{-1} $\leq v_s \leq$ 100 km s^{-1}, $\phi_{H\beta}$ is constant to $\pm 15\%$ rms. Using this result, we determine from the echelle spectrum that $\rho v_s^2 = 4.3 \times 10^{-10}$ dyn cm^{-2} at this location. For $v_s = 80$ km s^{-1}, this corresponds to $n_0 = 3.4$ cm^{-3} intermediate between the densities estimated for the radiative and nonradiative shocks nearby. This pressure is a factor of 1.8 below the pressure for the Balmer-dominated shocks as determined from the best-fit shock reflection model, and a factor of 1.7 higher than the derived ram pressure before the blast wave hit the cavity wall. The pressure at this location is a factor of 4.4 below the value determined for the "spur" filament studied by Raymond et al. (1988).

The echelle slit also crosses a knot of relatively bright Hα emission on its western end. Emission from [O III] is not strong here. This feature is visible in the spectrogram as two knots of emission at $v_r \approx 40$–50 km s^{-1}. At this location neither the morphology of the emission nor the velocity structure seem consistent with a simple smooth sheet. Rather, this may be a bow shock–like structure where the shock has encountered a well-defined knot of gas.

The morphology of this region definitely sets it apart from both the Balmer-dominated emission and the radiative shocks which make up the bright northeast limb of the Cygnus Loop. The structure is much less well ordered and suggestive of turbulence or some other chaotic process. We suggest two possibilities to account for the morphology of this region. The first is that since we are looking at material in the vicinity of the intersection of the blast wave and the cloud responsible for the bright northeast limb, we may be seeing turbulence associated with dynamical instabilities such as the Kelvin-Helmholtz instability which appear in numerical simulations of shocks encountering dense clouds (e.g. Klein, McKee, & Colella 1991).

The second possibility is that the flow behind these shocks is thermally unstable, allowing parcels of gas to drop out of pressure equilibrium with their surroundings, then be reshocked (e.g., Innes et al. 1987; Gaetz et al. 1988; Innes 1992). However, nothing about these shocks apart from their morphology itself sets them apart from other regions where order is better maintained. The range of shock velocities, preshock densities, and pressures seems to lie well within the range of parameters seen throughout the remnant. Furthermore, the shock velocities present in the region of the Balmer-dominated filaments fall in the range predicted to be most unstable, and yet this is clearly the most "well-behaved" region studied in the Cygnus loop.

On the other hand, it takes time for these instabilities to develop. In § 4.5 we suggest that such thermal instabilities may be responsible for a few regions of clumpy [O III] emission intermingled with the Balmer-dominated filaments. Might regions such as these in time develop to resemble the emission in the "intermediate" region? The sequence along the surface of the shock from the Balmer-dominated emission to the intermediate region to the radiative northeast limb (see Fig. 12) suggests that this might be an evolutionary sequence. Localized regions of slightly higher density such as filaments 1 and 2 may develop over time into regions such as the bright [O III] complexes. Then, as these regions accumulate larger column depths and as a large fraction of the surface of the blast wave starts to go radiative, the character of the shock could come to resemble the intermediate region discussed here.

5. SUMMARY

We have presented a suite of observational data on the Balmer-dominated northeast limb of the Cygnus Loop SNR, together with models of the kinetic properties of the shocked gas, the emission spectrum of the shocks, and the dynamical history of the region. Data presented include Hα, [O III], and X-ray images, UV and visible spectrophotometry, and high-resolution spectroscopy.

Our basic conclusions are as follows.

1. We find that the shock wave responsible for the Balmer-dominated emission in the northeast Cygnus Loop has undergone significant deceleration in the past few hundred to 1000 yr, and that the time scales for shock deceleration, postshock cooling, and the dynamical evolution of the region are all comparable. In particular, this greatly complicates comparison of observed line strengths with the predictions of steady flow shock models.

2. The two relatively bright Balmer-dominated filaments visible on the POSS prints are seen to be part of a very smooth and regular complex of filaments. These filaments mark the current location of the blast wave and are seen to bound the sharply limb-brightened X-ray emission, including the X-ray "halo" previously reported by Ku et al. (1984). The extremely regular character of the emission requires that the preshock medium be very uniform.

3. Inferences about the geometry of the region based on line profiles, together with the observed surface brightness of the emission, suggest a limit of less than 3 cm^{-3} for the current preshock density of filament 1. This is consistent with the density estimated by RBFG, but somewhat below the estimate of Long et al. (1992) based on O VI data. The high O VI surface brightness may be due to a greater than expected column of O VI arising from the velocity history of the shock.

4. The [O III]/Hβ ratio throughout the region is $\sim$0.1, except for regions in which the shock is undergoing a transition from being nonradiative to becoming an incomplete radiative shock. In such cases the [O III]/Hβ ratio can exceed 100. The transition from nonradiative to radiative shocks is found in three contexts within the field: a few discrete $\sim 10^{-18}$ cm clouds which have been recently shocked by the blast wave; portions of the otherwise Balmer-dominated blast wave which are just turning radiative; and a region of morphologically peculiar emission between the Balmer-dominated emission and the bright radiative northeast limb.

5. The transition from the nonradiative shock to a radiative shock is best seen along the length of filament 2, the northwestern of the two brightest filaments. Here the shock velocity and swept up column appear to go from $\sim$180 km s^{-1} and 10^{17} cm^{-2} at the southeast end of the filament to $\sim$140 km s^{-1} and 8×10^{17} cm^{-2} at the northwest end (although determination of these values is somewhat ambiguous because of the possibility of ongoing shock deceleration).

6. Balmer-dominated emission is observed to weaken and finally disappear as the strength of radiative [O III] emission increases (e.g., the increase in [O III] and the decline at Hα at the midpoint of filament 2). This is due to photoionization of the preshock medium by UV from the nascent cooling region. Model calculations confirm that the UV shock precursor is able to fully ionize the preshock medium at about the same column depth where significant [O III] emission from the cooling region is seen.

7. We are able to consistently interpret the current shock

velocity, the current pressure as inferred from the Hα surface brightness, the swept-up column depth, the X-ray temperature, the X-ray pressure, and the steepness of the X-ray limb brightening in terms of a model in which the Cygnus Loop blast wave encountered the wall of the preexisting cavity ~1000 yr. ago. The density inside the cavity was ~0.09 cm^{-3}. The current preshock density (the density of the cavity wall) is ~1.2 cm^{-3}. The current ram pressure, which is the pressure between the blast wave and the reflected shock, is $\sim 8 \times 10^{-10}$ dyn cm^{-2}. This is a factor of 3 higher than the pressure behind the blast wave prior to hitting the cavity wall. The success of this analysis supports the view that the Cygnus Loop was a cavity explosion. Our model is an oversimplification of the real situation in which the shock is running up a steep density gradient on the inside edge of the cavity wall.

8. Emission from the region between the blast wave and the reflected shock in lines such as O VI and N V may contribute to the strength of these lines UV spectra, thereby complicating their use in inferring shock velocities and preshock densities.

9. We predict that the X-ray limb should continue to brighten and become wider for the next 1000 yr or so as the reflected shock propagates back through the material previously swept up by the adiabatic blast wave. Since the morphology of filaments 1 and 2 indicates that preshock conditions at these locations (which are beginning to become radiative) cannot differ greatly from those of neighboring Balmer-dominated shocks, we conclude that the entire region is probably on the verge of becoming radiative. We expect that shocks throughout the region will undergo a radiative transition on the same time scale as the evolution of the X-ray brightness, during which time the Balmer-dominated northeast limb will come to resemble the radiative northeast or west limbs of the remnant.

10. High-resolution spectroscopy of the Hα line profile shows that the broad component is surprisingly narrow (~135 km s^{-1}). Consistency between this line width and the shock velocity inferred from spectrophotometry requires either rapid postshock equilibration of T_i and T_e, or that the shock front has decelerated from 180 km s^{-1} to 135 km s^{-1} in the last ~200 yr. While we cannot unambiguously distinguish between these models, the rate of deceleration required is consistent with an extrapolation of the deceleration rate inferred in (7) above.

11. The width of the narrow component of the Hα line profile is ~33 km s^{-1}. We are unable to account for this width by radiative transfer effects, which indicates that the preshock medium has been heated to ~25,000 K by a shock precursor. A number of possible precursor types are considered, most of which are troubled by the fact that they heat electrons and ionize H more efficiently that they heat preshock neutrals. The most promising types of precursor seem to be heating by fast postshock neutrals which overtake the shock or by cosmic rays. We find a lower limit to the cosmic-ray diffusion coefficient of 10^{23} cm^2 s^{-1} and a model-dependent upper limit of 10^{25} cm^2 s^{-1}. Regardless of the exact nature of the precursor, the heating of the preshock medium is capable of explaining the weak [S II] and [N II] emission previously reported by FI.

12. Morphologically peculiar emission located between the Balmer-dominated filaments and the radiative northeast limb consists of radiative shocks which are less well ordered than the Balmer-dominated region. Interpretation of echelle data give $\rho v_s^2 \approx 4.3 \times 10^{-10}$ dyn cm^{-2} for this region, intermediate between the current pressure inferred for the Balmer-dominated shocks and the pressure prior to the blast wave/cavity wall encounter. This may be a region of more chaotic flow around the edges of the cloud responsible for the bright radiative northeast limb. Alternatively, this region may represent a phase in the evolution of the Balmer-dominated blast wave as it accumulates more column depth and thermally unstable cooling sets in.

This work was supported at ASU by NASA/JPL contracts 959289 and 959329 and Caltech contract PC064528, at CfA by NASA grants NAG-528 and NAS5-87, and at JHU by NASA grant NAG5-988. Data were obtained in part with the Palomar 1.5 m telescope, which is jointly operated by the California Institute of Technology and the Carnegie Institution of Washington. J. J. H. would also like to acknowledge support from IPAC during his tenure there. We thank Knox Long for communication of the HUT results prior to publication.

REFERENCES

Aldcroft, T. L., Romani, R. W., & Cordes, M. 1992, ApJ, 400, 638
Ballet, J., Caplan, J., Rothenflug, R., Dubreuil, D., & Soutoul, A. 1989, A&A, 211, 217
Benvenuti, P., Dopita, M. A., & D'Odorico, S. 1980, ApJ, 238, 601
Blair, W. P., Long, K. S., Vancura, O., & Holberg, J. B. 1991a, ApJ, 374, 202
Blair, W. P., et al. 1991b, ApJ, 379, L33
Blandford, R. D., & Eichler, D. 1987, Phys. Rep., 154, 1
Boggess, A., et al. 1978, Nature, 275, 372
Boulares, A., & Cox, D. P. 1988, ApJ, 333, 198
Braun, R., & Strom, R. G. 1986, A&A, 164, 208
Cargill, P. J., & Papadopoulos, K. 1988, ApJ, 329, L29
Charles, P. A., Kahn, S. M., & McKee, C. F. 1985, ApJ, 295, 456
Chevalier, R. A., Kirshner, R. P., & Raymond, J. C. 1980, ApJ, 235, 186
Chevalier, R. A., & Raymond, J. C. 1978, ApJ, 225, L27
Cox, D. P. 1972a, ApJ, 178, 143
———. 1972b, ApJ, 178, 159
Cox, D. P., & Raymond, J. C. 1985, ApJ, 298, 651
Dopita, M. A. 1977, ApJS, 33, 437
Draine, B. T. 1980, ApJ, 241, 1021
Fesen, R. A., & Itoh, H. 1985, ApJ, 295, 43 (FI)
Fesen, R. A., Kwitter, K. B., & Downes, R. A. 1992, AJ, 104, 719
Gaetz, T. J., Edgar, R. J., & Chevalier, R. A. 1988, ApJ, 329, 927
Graham, J. R., Wright, G. S., Hester, J. J., & Longmore, A. J. 1991, AJ, 101, 175
Green, D. A. 1990, AJ, 100, 1927
Hanson, G. J., & Winkler, P. F., Jr. 1992, BAAS, 24, 1231
Hester, J. J. 1987, ApJ, 314, 187
Hester, J. J., & Cox, D. P. 1986, ApJ, 300, 675
Hester, J. J., Parker, R. A. R., & Dufour, R. J. 1984, ApJ, 273, 219
Hester, J. J., & Raymond, J. C. 1988, in Supernova Remnants and the Interstellar Medium, ed. R. S. Roger & T. L. Landecker (Cambridge: Cambridge Univ. Press), 415
Hester, J. J., Raymond, J. C., & Danielson, G. E. 1986, ApJ, 303, L17
Innes, D. E. 1992, A&A, 256, 660
Innes, D. E., Giddings, J. R., & Falle, S. A. E. G. 1986, in Workshop on Model Nebulae, ed. D. Pequinot (Paris: Observatorie), 153
Klein, R. I., McKee, C. F., & Colella, P. 1991, in Supernovae, ed. S. E. Woosley (New York: Springer), 696
Ku, W. H.-M., Kahn, S. M., Pisarski, R., & Long, K. S. 1984, ApJ, 278, 615
Kulkarni, S. R., & Hester, J. J. 1988, Nature, 335, 801
Long, K. S., Blair, W. P., Vancura, O., Bowers, C. W., Davidsen, A. F., & Raymond, J. C 1992, ApJ, 400, 214
McCray, R., & Snow, T. P. 1979, ARA&A, 17, 213
McKee, C. F., & Cowie, L. L. 1975, ApJ, 195, 715
Minkowski, R. 1958, Rev. Mod. Phys., 30, 1048
Osterbrock, D. E. 1989, Astrophysics of Gaseous Nebulae and Active Galactic Nuclei (Mill Valley, CA: University Science Books)
Parker, R. A. R. 1967, ApJ, 149, 363
Panek, R. J. 1982, NASA IUE Newletter, 18, 68
Rasmussen, A., & Martin, C. 1992, ApJ, 396, L103
Raymond, J. C. 1979, ApJS, 39, 1
———. 1991, PASP, 103, 666
Raymond, J. C., Black, J. H., Dupree, A. K., Hartmann, L., & Wolff, R. S. 1980a, ApJ, 238, 881
Raymond, J. C., Blair, W. P., Fesen, R. A., & Gull, T. R. 1983, ApJ, 275, 636 (RBFG)
Raymond, J. C., Davis, M., Gull, T. R., & Parker, R. A. R. 1980b, ApJ, 238, L21

Raymond, J. C., Hester, J. J., Cox, D. P., Blair, W. P., Fesen, R. A., & Gull, T. R. 1988, ApJ, 324, 869
Raymond, J. C., Wallerstein, G., & Balick, B. 1991, ApJ, 383, 226
Seab, C. B., & Shull, J. M. 1983, ApJ, 275, 652
Seaton, M. J. 1979, MNRAS, 187, 73P
Shull, J. M., & McKee, C. F. 1979, ApJ, 227, 131
Shull, P. O., Dyson, J. E., Kahn, F. D., & West, K. A. 1985, MNRAS, 212, 799
Smith, R. C., Kirshner, R. P., Blair, W. P., & Winkler, P. F. 1991, ApJ, 375, 652
Smith, R. C., Laming, M. L., & Raymond, J. C. 1993a, in preparation
Smith, R. C., Raymond, J. C., & Laming, M. L. 1993b, in press
Spitzer, L., Jr. 1978, Physical Processes in the Interstellar Medium (New York: Wiley)
Teske, R. G., & Kirshner, R. P. 1985, ApJ, 292, 22
Treffers, R. R. 1981, ApJ, 250, 213
Tucker, W. 1971, Science, 172, 372
Zel'dovich, Y. B., & Raizer, Y. P. 1968, Elements of Gas Dynamics and the Classical Theory of Shock Waves (New York: Scripta Technica)